
A hybrid multi-time-step framework for pore-scale and continuum-scale modeling of solute transport in porous media

AUTHORED BY

S. KARIMI

Graduate Student, University of Houston.

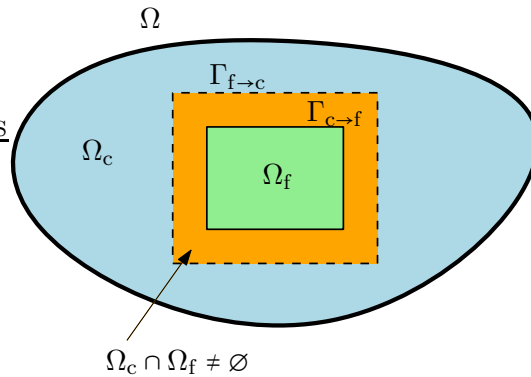
K. B. NAKSHATRALA

Department of Civil & Environmental Engineering

University of Houston, Houston, Texas 77204-4003.

phone: +1-713-743-4418, **e-mail:** knakshatrala@uh.edu

website: <http://www.cive.uh.edu/faculty/nakshatrala>



The proposed coupling method employs overlapping domain decomposition. This figure illustrates the partitioning of the computational domain Ω into subdomains in which continuum-scale and pore-scale features are sought after.

A hybrid multi-time-step framework for pore-scale and continuum-scale modeling of solute transport in porous media

S. Karimi and K. B. Nakshatrala

Department of Civil and Environmental Engineering, University of Houston.

Correspondence to: knakshatrala@uh.edu

ABSTRACT. Understanding transport processes in porous media is vital to many scientific and industrial applications. For instance, predicting the fate of chemical contaminants in subsurface, and simulating various processes in geological carbon-dioxide sequestration are two of the most prominent examples. Considering the dimensions of a typical spatial domain in such problems, usually in the order of kilometers, continuum models based on averaging theories have been the dominant approaches toward simulation of the above-mentioned processes. However, a variety of interactions among the involved chemical species at the pores (such as dissolution and precipitation) cannot be accounted within the current continuum-scale models. To include these features into a computational model, one needs to opt for length- and time-scales that are much smaller than the ones typically considered for a field-scale model. Capturing such disparate temporal and spatial scales still remains an enduring challenge in computational mechanics. No single numerical method can efficiently bridge the gap between these disparate scales. Hence, designing numerical methodologies that employ different numerical methods in different regions have grown into a major topic of interest among researchers.

In this paper, we propose a computational framework, which is based on a domain decomposition technique, to employ both finite element method (which is a popular continuum modeling approach) and lattice Boltzmann method (which is a popular pore-scale modeling approach) in the same computational domain. To bridge the gap across the disparate length and time-scales, we first propose a new method to enforce continuum-scale boundary conditions (i.e., Dirichlet and Neumann boundary conditions) onto the numerical solution from the lattice Boltzmann method. This method are based on maximization of entropy and preserve the non-negativity of discrete distributions under the lattice Boltzmann method. The proposed computational framework allows different grid sizes, orders of interpolation, and time-steps in different subdomains. This allows for different desired resolutions in the numerical solution in different subdomains. Through numerical experiments, the effect of grid and time-step refinement, disparity of time-steps in different subdomains, domain partitioning, and the number of iteration steps on the accuracy and rate of convergence of the proposed methodology are studied. Finally, to showcase the performance of this framework in porous media applications, we use it to simulate the dissolution of calcium carbonate in a porous structure.

Key words and phrases. hybrid methods; multi-time-step schemes; pore-scale modeling; multi-scale methods; advective-diffusive-reactive systems; partitioned schemes; lattice Boltzmann method.

1. INTRODUCTION AND MOTIVATION

Transport of chemical species in porous media features a wide variety of time- and length-scales. Reaction and precipitation at the interface of fluid and solid [Bekri et al., 1995; Noorden and Pop, 2008; Wood et al., 2007], reactive flow and transport [Shapiro and Brenner, 1986], and varied dynamics of (bio-)chemical reactions [Murphy and Ginn, 2000] are a few of the processes that occur at disparate scales. The three length-scales that are typically considered in the study on porous media are pore-scale (also referred to as fine-scale or micro-scale), meso-scale (also referred to as continuum-scale or coarse-scale) and macro-scale (also referred to as field-scale). The properties of interest depend on the scale of observation, which implies that different modeling approaches are needed at different scales. Moreover, a numerical method appropriate for a particular length- or time-scale need not be a viable approach at a different scale. Due to this scale disparity, as shown in figure 1, the choice of a particular modeling approach or a particular numerical methodology that is appropriate for all the scales of observation is severely limited.

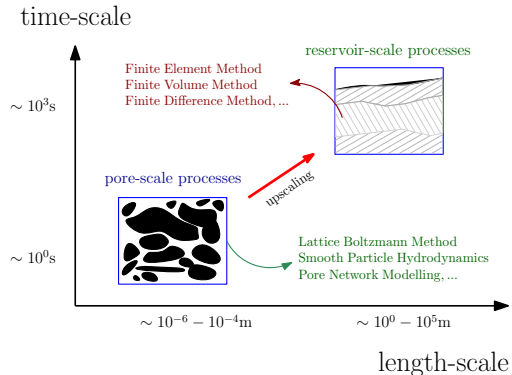


FIGURE 1. This figure illustrates the disparity in time- and length-scales in porous media simulations.

1.1. Coarse-scale modeling. Finite Element Method (FEM), Finite Volume Method (FVM) and Finite Difference Method (FDM) are commonly practiced schemes for coarse-scale fluid dynamics computations. However, fine-scale features may not be immediately included into the numerical solutions from these methods. Some of the efforts towards improving upon this shortcoming are the Variational Multi-Scale method in [Hughes et al., 1998], Generalized Finite Element Method [Melenk and Babuška, 1996], Multi-Scale Finite Element Method [Hou and Wu, 1997], which can include some fine-scale spatial features into the finite element solution via manipulation of interpolation functions or the weak formulation. Although coarse-scale models can be solved in a computationally efficient manner and can include some limited fine-scale features, these models are not capable of capturing all the important pore-scale processes and their impact at the meso-scale and field-scale [Gramling et al., 2002]. The source of this deficiency is, partly, the dependence of the model parameters on the length-scale. Furthermore, some processes in reactive-transport (e.g., some pore-scale reactions) cannot be upscaled from pore-scale to meso-scale [Battiato et al., 2009].

1.2. Pore-scale modeling. Methods such as pore network modeling [Fatt, 1956], Smooth Particle Hydrodynamics (SPH) [Monaghan, 2005] and the Lattice Boltzmann Method (LBM) [Chen and Doolen, 1998] are amongst the most popular methods for fine-scale simulations. In particular, LBM offers great potential in including kinetic and atomistic details into the computational model. This fact originates from the main purpose of LBM, which is to numerically solve the Boltzmann equation [He and Luo, 1997]. This equation can describe the distribution of particles of a system in the phase space at any thermodynamic state. Sophisticated gas-interface interaction models [Cercignani, 1988; Cercignani and Lampis, 1971] and kinetic relations can also be included in the solution of the Boltzmann equation [Cercignani, 1988; Cercignani et al., 2013]. *Despite the advantages of LBM over*

coarse-scale methods such as FEM or FVM, its application to real-world problems in subsurface modeling is impractical due to prohibitive computational cost.

1.3. Hybrid modeling. It is now becoming evident that a viable approach for simulation of reactive-transport in porous media should consist of both fine-scale and coarse-scale models; for example, see the discussion in [Scheibe et al., 2015]. The modeling approaches that employ both fine-scale and coarse-scale models are collectively referred to as *hybrid* modeling. The motivation for hybrid modeling is four-fold:

- (i) There is a need for increasing local modeling accuracy in certain applications. Some examples include flow and transport along thin fractures, and to model processes in the well-bore cement that may act as escape passages for carbon-dioxide in geological carbon sequestration.
- (ii) The need for hybrid modeling can arise when continuum assumptions locally break down in critical parts of the domain. For example, reactive-transport modeling under advection-dominated or reaction-dominated conditions, as described in [Battiato et al., 2011].
- (iii) The need for incorporating effects of the surrounding media on the subdomain for accurate predictions of flow and transport [Sun et al., 2012].
- (iv) To achieve a manageable computational cost to solve realistic problems arising in subsurface applications.

Recently, there is a surge in research activity in hybrid modeling. A non-iterative coupling method for SPH and coarse-scale averaged SPH was proposed in [Tartakovsky et al., 2008] for advection-diffusion-reaction equation and precipitation in porous media. Using SPH for different length-scales allows the mentioned method to avoid predictor-corrector iterations in each time-step. The multi-scale algorithm proposed in [Battiato et al., 2011] is based on FVM and uses an iterative approach to resolve the disparate length-scales in a transport process. In [Balhoff et al., 2008] coupling of finite element method and pore network modeling for flow problems in porous media, using the mortar method was introduced for the first time. This method was then extended in [Mehmani and Balhoff, 2014] to couple FDM and pore network model for simulation of flow and transport of chemical species. It utilizes the mortar finite element spaces to transfer information from one subdomain to another. The unknowns are updated iteratively to satisfy continuity of fluxes at the interface within a user-defined tolerance. In [Tang et al., 2015], these mortar-based methods are used to couple finite difference and cellular automata methods to model the bio-film development in porous media. Coupling of FDM and LBM for advection-diffusion equation is studied in [Albuquerque et al., 2004], but non-matching grids and disparate time-steps are not considered. A hybrid method that incorporates LBM and FEM for simulation of the diffusion processes is proposed in [Haslam et al., 2008]. A more recent effort in this direction is given in [Astorino et al., 2014] that allows different time-steps and grid sizes for FEM and LBM domains.

1.4. Multiple temporal scales and multi-time-step methods. Multi-time-step (multi-rate) methods aim at resolving the disparity in time-scales in a system through use of appropriate time-steps and time-integrators for each subsystem. In recent years, development of multi-time-step methods has received much attention among researchers of various fields. These include: multi-rate methods based on Runge-Kutta schemes [Constantinescu and Sandu, 2013; Günther et al., 2001], adaptive variational integrators for dynamics [Lew et al., 2004], multi-time-step methods based on non-overlapping domain decomposition [Karimi and Nakshatrala, 2014, 2015a], and symplectic multi-time-step methods for molecular dynamics simulations [Bridges and Reich, 2001; Leimkuhler and Reich,

2004]. Multi-time-step coupling algorithms based on domain partitioning are often classified as either *staggered* or *monolithic* coupling schemes [Nakshatrala et al., 2008]. Staggered coupling methods update the solution in different subdomains through a predictor-corrector procedure. Hence, there is a time-lag between the solutions at different subdomains, which can result in numerical instabilities. However, this type of algorithms enjoy tremendous popularity because of modularity; one can employ available solvers and use them (with different time-steps) in a staggered coupling algorithm without any major modification. Unlike staggered coupling algorithms, monolithic schemes update the solution in the entire domain using a single iteration. There is no time-lag between the solution of different subdomains. As a result, monolithic coupling algorithms enjoy much better numerical stability than staggered coupling methods. However, current numerical solvers for partial differential equations cannot be immediately included in a monolithic coupling scheme and a major effort in developing computer codes is required. Also, multi-time-step integration requires careful design of a coupling algorithm [Karimi and Nakshatrala, 2014]. Due to the aforementioned reasons, we shall employ a staggered coupling approach.

1.5. Domain decomposition methods. A natural way to develop a staggered coupling method is to employ domain decomposition techniques, which also offer an attractive framework for parallel computing. Over the years, a variety of overlapping and non-overlapping domain decomposition techniques have been developed [Mathew, 2008; Quarteroni and Valli, 1999; Toselli and Widlund, 2005]. These methods have the potential to employ non-matching computational grids in different subdomains; for instance, mortar finite element spaces [Arbogast et al., 2007; Wohlmuth, 2000] and overlapping methods [Cai and Saad, 1996; Lions, 1988] are among them. However, having different grid-sizes in different subdomains may not be enough to account for disparate time-scales that can be present in the model problem. In order to achieve computational efficiency for problems involving multiple temporal scales, one needs to employ tailored numerical time-integrators and time-steps for each active process. That is, domain decomposition techniques and multi-time-stepping schemes go hand in hand. Herein, we employ overlapping domain decomposition technique whose advantages will be discussed later.

1.6. An outline of the paper. We provide an overview of our approach in Section 2. Section 3 provides the governing equations at the continuum-scale and the associated numerical modeling. Section 4 discusses the modeling at the pore-scale using the lattice Boltzmann method. An overview of overlapping domain decomposition techniques and information transfer across non-matching grids is given in Section 5. In Section 6, we present a robust hybrid multi-time-step coupling method that allows to couple pore-scale and continuum-scale subdomains. Section 7 presents several numerical results using the proposed hybrid modeling, and illustrates the robustness and utility of the proposed computational framework. Finally, conclusions are drawn in Section 8 along with a discussion on possible future research endeavors in the area of hybrid modeling.

2. AN OVERVIEW OF OUR APPROACH

In this paper, we present a hybrid method to couple the advection-diffusion equation at the continuum-scale with the Boltzmann equation at the pore-scale to simulate the transport of chemical species. The proposed method can capture fine-scale features and processes by solving the lattice Boltzmann equation at the pore-scale. The response at the continuum-scale is captured by solving the advection-diffusion equation using the finite element method.

We use the domain decomposition technique to partition the computational domain into *fine-scale* and *coarse-scale* subdomains. For better numerical stability, we allow the coarse-scale and fine-scale computational subdomains to overlap, and appropriate boundary conditions are designed at the boundary of the individual computational subdomains. To capture disparate time-scale, the proposed computational framework allows different time-steps and different time integration algorithms in different subdomains. Furthermore, computational grids and different orders of interpolation can be employed in different subdomains. This enables the user to choose appropriate time-step, mesh and interpolation in each subdomain for stability and desired accuracy.

The first step in a hybrid simulation using the proposed framework is to partition the computational domain into regions for fine-scale and coarse-scale modeling by identifying the regions where pore-scale analysis is needed. Thanks to the design of the proposed framework, creating computational meshes for these two types of subdomains is easy and can be carried out independent of each other. Finally, the analysis is carried out by using appropriate models in different subdomains. The overall procedure is summarized in figure 2. Some of the salient features of the proposed framework are as follows:

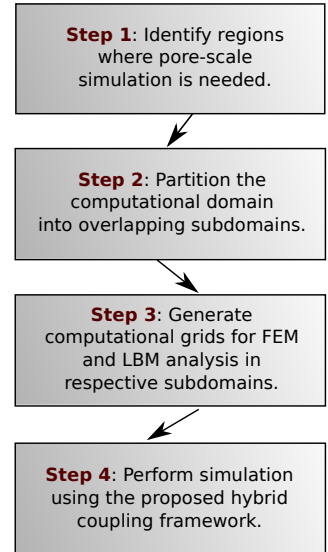


FIGURE 2. The main steps under the proposed hybrid framework.

- (i) Various transport processes and reactions can be incorporated into the analysis. In particular, the user can include complex advection velocity field (which is encountered frequently in porous media applications) and cascade of geochemical reactions without any change in the design of the coupling framework.
- (ii) One can divide the computational domain into multiple subdomains, and can independently employ in each subdomain either pore-scale modeling or continuum-scale modeling.
- (iii) The computational grids in a subdomain need not conform with the computational grid in another subdomain. In particular, the finite element mesh in the continuum-scale modeling need not match with the lattice structure in the lattice Boltzmann method, which is employed in the pore-scale analysis. This provides a great degree of flexibility for the modelers.
 - (a) One can employ meshes with different degrees of approximation independent of other subdomains. There is no need for compatibility among the interpolation spaces (e.g., mortar spaces) along the subdomain interfaces.
 - (b) This allows to leverage on the existing computational methods for modeling at pore-scale and continuum-scale. There is no need to design new methods just to be compatible with the hybrid coupling.
- (iv) One can employ different time-steps and different time stepping schemes in different subdomains, which is an attractive feature to possess for solving problems involving multiple temporal scales.
- (v) An accurate transfer of data across non-matching grids has been incorporated into the proposed computational framework.

- (vi) A novel way of implementing boundary conditions has been developed for the discretization under the lattice Boltzmann method. This enhances the accuracy at the pore-scale, and hence the overall accuracy of a hybrid coupling.
- (vii) No initial guess at the interface of subdomains is needed. Hence, implementation is easier and the simulation procedure can be fully automated.

In order to achieve aforementioned features, the computational framework is developed by integrating the following main ingredients:

- (a) A solver for continuum-scale modeling, which in our case will be a finite element formulation for advection-diffusion/dispersion equations.
- (b) A solver for pore-scale modeling, which in our case will be the lattice Boltzmann method with an improved discretization of boundary conditions.
- (c) An overlapping domain decomposition framework.
- (d) An accurate algorithm to transfer scalars, vectors and tensors across non-matching computational grids.
- (e) An iterative coupling algorithm to ensure compatibility of solution across the overlapping region.

A computational framework with the aforementioned features, which is essential to gain a fundamental understanding of subsurface processes, is currently not available. We therefore strive to design such a framework in this paper. The details of the aforementioned ingredients along with the illustration of the performance of the proposed hybrid multi-time-step computational framework are provided in subsequent sections.

3. CONTINUUM-SCALE MODELING

We shall model the transport at the continuum-scale using unsteady advection-dispersion equations. To this end, consider a bounded open domain $\Omega_c \subset \mathbb{R}^{nd}$ on which we seek to perform continuum modeling, where \mathbb{R} denotes the set of real numbers and “ nd ” is the number of spatial dimensions. We assume that the boundary of this domain, $\partial\Omega_c$, is comprised of Γ_c^N and Γ_c^D such that we have

$$\partial\Omega_c = \Gamma_c^N \cup \Gamma_c^D \quad \text{and} \quad \Gamma_c^D \cap \Gamma_c^N = \emptyset \quad (3.1)$$

Dirichlet boundary conditions are enforced on Γ_c^D , and Neumann boundary conditions are enforced on Γ_c^N . A spatial point in Ω_c will be denoted by \mathbf{x} . We use $\text{div}[\cdot]$ and $\text{grad}[\cdot]$, respectively, to denote the spatial divergence and gradient operators. The time interval of interest is denoted by $\mathcal{I} = (0, T]$, and the time is denoted by t . The initial boundary value problem at the continuum-scale can be written as follows:

$$\frac{\partial \mathbf{u}}{\partial t} + \text{div}[\mathbf{v}\mathbf{u} - D\text{grad}[\mathbf{u}]] = s \quad (\mathbf{x}, t) \in \Omega_c \times \mathcal{I} \quad (3.2a)$$

$$\mathbf{u}(\mathbf{x}, t = 0) = \mathbf{u}_0(\mathbf{x}) \quad \mathbf{x} \in \Omega_c \quad (3.2b)$$

$$\mathbf{u}(\mathbf{x}, t) = \mathbf{u}^p(\mathbf{x}, t) \quad (\mathbf{x}, t) \in \Gamma_c^D \times \mathcal{I} \quad (3.2c)$$

$$\hat{\mathbf{n}} \cdot (\mathbf{v}\mathbf{u} - D\text{grad}[\mathbf{u}]) = \mathbf{q}^p \quad (\mathbf{x}, t) \in \Gamma_c^N \times \mathcal{I} \quad (3.2d)$$

where \mathbf{u} is the concentration, \mathbf{v} is the divergence-free advection velocity (i.e., $\text{div}[\mathbf{v}] = 0$ in Ω_c), D is the dispersion coefficient, and s is the source/sink term. Although the dependence is not explicitly indicated, all of the mentioned quantities depend on the spatial coordinates and time. The dispersion coefficient D is positive and can be spatially heterogeneous. The initial concentration in

Ω_c is denoted by u_0 , and u^P is the prescribed concentration on Γ_c^D . The outward unit normal to $\partial\Omega_c$ is denoted by $\hat{\mathbf{n}}$, and q^P is the prescribed flux on Γ_c^N .

The solution to the above equations can exhibit disparate spatial and temporal scales, which depend on the relative strengths of advection, dispersion and reaction processes, and volumetric source [Gresho and Sani, 2000; Hundsdrofer and Verwer, 2007]. We employ the finite element method for the numerical modeling at the continuum-scale.

3.1. The finite element method. We shall introduce the following function spaces:

$$\mathbf{C} := \left\{ \mathbf{u} : \Omega_c \times \mathcal{I} \rightarrow \mathbb{R} \mid \mathbf{u}(\mathbf{x}, t) \in H^1(\Omega_c) \text{ and } \mathbf{u}(\mathbf{x} \in \Gamma_c^D, t) = u^P \ \forall t \in \mathcal{I} \right\} \quad (3.3a)$$

$$\mathbf{W} := \left\{ \mathbf{w} : \Omega_c \rightarrow \mathbb{R} \mid \mathbf{w}(\mathbf{x}) \in H^1(\Omega_c) \text{ and } \mathbf{w}(\mathbf{x} \in \Gamma_c^D) = 0 \right\} \quad (3.3b)$$

where $H^1(\Omega_c)$ is a Sobolev space defined on Ω_c [Evans, 1998]. We shall denote the standard L_2 inner product over a set \mathcal{K} as follows:

$$(\mathbf{w}, \mathbf{u})_{\mathcal{K}} \equiv \int_{\mathcal{K}} \mathbf{w} \cdot \mathbf{u} \, d\mathcal{K} \quad (3.4)$$

For convenience, we shall drop the subscript \mathcal{K} if $\mathcal{K} = \Omega_c$. We shall employ the semi-discrete methodology to decouple the spatial and temporal discretizations [Zienkiewicz and Taylor, 1977]. There are a multitude of ways to construct a weak formulation for equations (3.2a)–(3.2d). In this paper, we shall limit to the Galerkin formulation and the Streamline Upwind/Petrov-Galerkin formulation [Franca et al., 1992]. However, it should be noted that any other finite element (or even a finite volume) formulation can also be employed in the modeling at the coarse-scale.

3.1.1. *The Galerkin formulation.* Find $\mathbf{u}(\mathbf{x}, t) \in \mathbf{C}$ such that we have

$$(\mathbf{w}, \partial\mathbf{u}/\partial t) + (\mathbf{w}, \mathbf{v} \cdot \text{grad}[\mathbf{u}]) + (\text{grad}[\mathbf{w}], \text{Dgrad}[\mathbf{u}]) = (\mathbf{w}, \mathbf{s}) + (\mathbf{w}, q^P)_{\Gamma_c^N} \quad \forall \mathbf{w} \in \mathbf{W} \quad (3.5a)$$

$$\mathbf{u} = u_0 \quad \forall \mathbf{x} \in \Omega_c, \ t = 0 \quad (3.5b)$$

$$\mathbf{u} = u^P \quad \forall (\mathbf{x}, t) \in \Gamma_c^D \times \mathcal{I} \quad (3.5c)$$

Note that the Dirichlet boundary conditions are enforced strongly. We shall employ the Galerkin formulation only for dispersion-dominated problems, as this formulation is known to perform poorly for advection-dominated problems. This shortcoming can be partly alleviated by employing a stabilized formulation instead.

3.1.2. *The Streamline Upwind/Petrov-Galerkin (SUPG) formulation.* The SUPG formulation is a popular stabilized formulation, and it reads as follows: Find $\mathbf{u}(\mathbf{x}, t) \in \mathbf{C}$ such that we have

$$\begin{aligned} & (\mathbf{w}, \partial\mathbf{u}/\partial t) + (\mathbf{w}, \mathbf{v} \cdot \text{grad}[\mathbf{u}]) + (\text{grad}[\mathbf{w}], \text{Dgrad}[\mathbf{u}]) \\ & + \sum_{e=1}^{N_{\text{FEM}}} (\mathbf{v} \cdot \text{grad}[\mathbf{w}], \tau_e \mathbf{R}[\mathbf{u}])_{\Omega_c^e} = (\mathbf{w}, \mathbf{s}) + (\mathbf{w}, q^P)_{\Gamma_c^N} \quad \forall \mathbf{w} \in \mathbf{W} \end{aligned} \quad (3.6)$$

where N_{FEM} is the total number of finite elements and τ_e is the stabilization parameter for element e . The spatial domain contained in element e is shown by Ω_c^e . The residual $\mathbf{R}[\mathbf{u}]$ is defined as follows:

$$\mathbf{R}[\mathbf{u}] = \frac{\partial\mathbf{u}}{\partial t} + \text{div}[\mathbf{v}\mathbf{u} - \text{Dgrad}[\mathbf{u}]] - \mathbf{s} \quad (3.7)$$

The Dirichlet boundary condition and initial condition will remain as in equation (3.5). We employ the stabilization parameter τ_e as given in [Augustin et al., 2011]. That is,

$$\tau_e = \frac{h_e}{2p \|\mathbf{v}\|} \chi(P_e^h), \quad P_e^h = \frac{\|\mathbf{v}\| h_e}{2pD}, \quad \chi(\alpha) = \coth(\alpha) - 1/\alpha \quad (3.8)$$

where p is the order of finite element interpolation functions and D is the *isotropic* coefficient of dispersion. The element size is denoted by h_e , and P_e^h is the element Péclet number.

4. PORE-SCALE MODELING: THE LATTICE BOLTZMANN METHOD

We shall use Ω_f to denote the region in which one seeks to perform pore-scale modeling. We use the Boltzmann equation to describe the transport processes at the pore-scale. The Boltzmann equation provides a statistical description of the state of matter away from the thermodynamic equilibrium [Cercignani, 1988]. This equation describes the evolution of the distribution of particles in the phase space, from which macroscopic variables can be easily computed by taking appropriate moments. If one neglects the external force term, the Boltzmann equation can be written as:

$$\frac{\partial f}{\partial t} + \mathbf{v} \cdot \text{grad}[f] = \mathcal{Q}[f, f^{\text{eq}}] \quad \text{in } \Omega_f \quad (4.1)$$

where f is the distribution function, \mathbf{v} is the macroscopic (or background) velocity, and \mathcal{Q} is the collision term. Herein, we will consider the Bhatnagar-Gross-Krook (BGK) collision model [Bhatnagar et al., 1954], which can be written as:

$$\mathcal{Q}[f, f^{\text{eq}}] = \frac{1}{\lambda} (f^{\text{eq}} - f) \quad (4.2)$$

where f^{eq} is the distribution of particles in the phase space at the thermodynamics equilibrium. The parameter λ is called the relaxation time. In this paper, we will use the Maxwell-Boltzmann distribution for the equilibrium distribution f^{eq} . That is,

$$f^{\text{eq}}(\mathbf{x}, \boldsymbol{\zeta}; \mathbf{v}, u) = \frac{u}{\sqrt{2\pi RT}} \exp[-(\boldsymbol{\zeta} - \mathbf{v}) \cdot (\boldsymbol{\zeta} - \mathbf{v})/2RT] \quad (4.3)$$

where $u(\mathbf{x}, t)$ is the concentration, R is the ideal gas constant, and T is the temperature. The velocity of particles is indicated by $\boldsymbol{\zeta}$.

In order to provide a complete description of the Boltzmann equation for a physical problem, appropriate boundary conditions have to be included. Fortunately, the mathematical theory of boundary conditions for Boltzmann equation is rather well-developed; for example, see [Cercignani, 1988; Cercignani and Lampis, 1971; Cercignani et al., 2013]. However, to use the existing theories to their full extent, one has to incorporate detailed dynamics for interaction between the particle and the surrounding surface of the domain. Obviously, the continuum model problem given in equation (3.2) lacks such information. Hence, the Boltzmann equation provides a much more powerful framework to account for detailed dynamics of gas-surface interaction that the continuum model is incapable of. In this paper, we will assume that the user merely intends to replicate the behavior of the macroscopic solution of equation (3.2) and an in-depth treatment of gas-surface interaction is of no interest. In the following, we will provide an overview of discretization of Boltzmann equation.

4.1. The lattice Boltzmann method. The lattice Boltzmann method is a popular numerical method to solve the Boltzmann equation (4.1). This method offers great potential for parallelization [Xian and Takayuki, 2011] and simulation in domains with complex spatial features [Succi, 2001]. We will employ standard lattice model $DnQm$ to discretize the velocity space. These discrete velocities are identified by vectors \mathbf{e}_i , $i = 1, \dots, m$. The discrete population corresponding to the lattice velocity \mathbf{e}_i is denoted by f_i . Considering the lattice cell size of h and a time-step Δt , the discrete form of Boltzmann equation can be written as:

$$|f_i\rangle(\mathbf{x} + \mathbf{e}_i\Delta t, t + \Delta t) = |f_i\rangle(\mathbf{x}, t) + |\mathcal{Q}_i\rangle(\mathbf{x}, t) \quad (4.4)$$

where the column vector of discrete populations is denoted using the Dirac notation $|\cdot\rangle$ [Lallemand and Luo, 2000]. Location of a lattice node is shown by \mathbf{x} and t is a discrete time-level. The discrete collision operator \mathcal{Q}_i is defined as:

$$|\mathcal{Q}_i\rangle(\mathbf{x}, t) = \frac{1}{\tau} (|f_i^{\text{eq}}\rangle(\mathbf{x}, t) - |f_i\rangle(\mathbf{x}, t)) \quad (4.5)$$

The non-dimensional relaxation-time is denoted by τ and is defined as:

$$\tau = \frac{1}{2} + \frac{D}{c_s^2\Delta t} \quad (4.6)$$

with c_s being the lattice sound velocity (e.g., in the case of $D2Q9$ lattice model $c_s = \Delta x/\sqrt{3}\Delta t$). For the equilibrium distribution in equation (4.5), we will employ the following approximation to the Maxwell-Boltzmann distribution in equation (4.3):

$$f_i^{\text{eq}}(\mathbf{x}, t; u) = w_i u \left(1 + \frac{\mathbf{e}_i \cdot \mathbf{v}}{c_s^2} + \frac{1}{2} \frac{(\mathbf{e}_i \cdot \mathbf{v})^2}{c_s^4} - \frac{\mathbf{v} \cdot \mathbf{v}}{c_s^2} \right) \quad (4.7)$$

where w_i is the weight associated with \mathbf{e}_i and \mathbf{v} is the advection velocity. Concentration is denoted by u . In the rest of the paper, we will assume that $\|\mathbf{v}\|/c_s \ll 1$ (low Mach number assumption). Macroscopic quantities of interest, in this case concentration and flux, can be obtained by the following relations

$$u(\mathbf{x}, t) = \sum_{i=1}^m f_i(\mathbf{x}, t) \quad (4.8a)$$

$$\mathbf{q}(\mathbf{x}, t) = \sum_{i=1}^m f_i(\mathbf{x}, t) \mathbf{e}_i \quad (4.8b)$$

Despite ever-growing popularity of lattice Boltzmann methods for computational fluid dynamics assumptions, these methods are prone to produce unphysical values for populations f_i ; for example, see [Karimi and Nakshatrala, 2015b]. Obviously, for equation (4.1) to be meaningful, the value of population f needs to be non-negative. Some of the approaches toward resolving this issue can be found in [Dellacherie, 2014; Karlin et al., 2006; Li et al., 2004]. Herein, we will propose a simple condition on the LBM discretization that guarantees non-negative values for discrete populations. We assume that the initial values for populations are also non-negative; for instance, this can be achieved if one takes $f_i(\mathbf{x}, t = 0) = f_i^{\text{eq}}(\mathbf{x}, t = 0)$. From equations (4.4) and (4.5) we can conclude that if $1 - 1/\tau \geq 0$, then the discrete populations at time-level $t + \Delta t$ will also be non-negative. Note that the streaming process does not contribute to negativity (an appropriate treatment of boundary conditions comes later). This condition leads to the following result

$$\Delta t \leq \frac{2D}{c_s^2} \quad (4.9)$$

For instance, in the case of a $D2Q9$ lattice model, one should have

$$h^2 \leq 6\Delta t D \quad (4.10)$$

The advantage of this method compared to methods such as entropic lattice Boltzmann method is that one does not need to solve a non-linear equation at each lattice node. Hence, it is much easier to code and computationally more efficient. Furthermore, the standard collision and streaming steps in the lattice Boltzmann method have remained untouched and no further modification is necessary.

To complete the description of lattice Boltzmann method for advection-diffusion equation, we need to demonstrate how to apply boundary conditions so that the resulting discrete populations are non-negative. In the following we will provide new methods for enforcing Dirichlet- and Neumann-type boundary conditions in equation (3.2).

4.1.1. *Boundary conditions for the lattice Boltzmann method.* Over the past few decades, a multitude of methods for enforcing macroscopic boundary conditions in the context of lattice Boltzmann methods for flow and transport equations have been proposed. For example, see [Chen et al., 2013; Skordos, 1993; Zou and He, 1997]. However, note that the boundary conditions typically considered for flow or transport problems in a macroscopic framework do not imply a unique configuration of particles in phase space. Another drawback of these methods can be that they may result in negative values for discrete populations. Other physical properties of the solution, such as monotonicity of entropy production may also be lost following enforcement of boundary conditions. Designing a numerical method to enforce boundary conditions appropriately, is indeed a challenging topic. Herein, to partially rectify the aforementioned problems, we propose a new framework for enforcing Dirichlet and Neumann boundary conditions for lattice Boltzmann method. These methods are based on the assumption that the system encompassed in domain Ω is connected to a bath of particles that reside in a specific state of thermodynamics equilibrium. This thermodynamic state can be identified by maximizing the entropy function, subject to a hydrodynamic constraint.

In this paper, we will utilize the Boltzmann's \mathcal{H} function to find the state of equilibrium. Obviously, the entropy \mathcal{S} is related to the \mathcal{H} function via the following relation:

$$\mathcal{S} = -\mathcal{H} \quad (4.11)$$

Hence, maximization of entropy \mathcal{S} is mathematically equivalent to minimizing \mathcal{H} . The \mathcal{H} function at each point is defined as:

$$\mathcal{H}(|f_i\rangle)|_{(\mathbf{x},t)} = \sum_{i=1}^m f_i(\mathbf{x},t) \log \left[\frac{f_i(\mathbf{x},t)}{w_i} \right] \quad (4.12)$$

For brevity, we will use the following notation:

$$\mathbf{M}^-(\mathbf{x}) := \{i \mid \mathbf{e}_i \cdot \widehat{\mathbf{n}}(\mathbf{x}) < 0, i = 1, \dots, m \text{ and } \mathbf{x} \in \partial\Omega\} \quad (4.13)$$

where $\widehat{\mathbf{n}}(\mathbf{x})$ is the unit outward normal to $\partial\Omega$. Obviously, the unknown populations near the boundary are f_i with $\mathbf{e}_i \in \mathbf{M}^-(\mathbf{x})$ for every point \mathbf{x} on $\partial\Omega$. The rest of the discrete populations are known from the collision and streaming steps prior to enforcement of boundary conditions.

- (a) *Dirichlet boundary condition*: Let $\mathbf{x} \in \Gamma^D$ and $u^P(\mathbf{x}, t)$ be the prescribed concentration at that point. The unknown populations are calculated by solving the following constrained optimization problem:

$$\min_{f_j, j \in M^-(\mathbf{x})} \mathcal{H}(|f_i|)|_{(\mathbf{x}, t)} \quad (4.14a)$$

$$\text{subject to } \sum_{i=1}^m f_i(\mathbf{x}, t) = u^P(\mathbf{x}, t) \quad (4.14b)$$

where the function \mathcal{H} is defined in equation (4.12). This minimization problem will result in the following relation:

$$\begin{aligned} f_i(\mathbf{x}, t) &= \frac{w_i}{\sum_{j \in M^-(\mathbf{x})} w_j} \left(u^P(\mathbf{x}, t) - \sum_{k \notin M^-(\mathbf{x})} f_k(\mathbf{x}, t) \right) \quad i \in M^-(\mathbf{x}) \\ f_i(\mathbf{x}, t) &\geq 0 \quad \forall i = 1, \dots, m \end{aligned} \quad (4.15)$$

Note that the function \mathcal{H} is only defined for non-negative arguments.

- (b) *Neumann boundary condition*: Let $\mathbf{x} \in \Gamma^N$ and $q^P(\mathbf{x}, t)$ be the prescribed flux at that point. The unknown populations are governed by the following constrained optimization problem:

$$\min_{f_j, j \in M^-(\mathbf{x})} \mathcal{H}(|f_i|)|_{(\mathbf{x}, t)} \quad (4.16a)$$

$$\text{subject to } \sum_{i=1}^m f_i(\mathbf{x}, t) \mathbf{e}_i \cdot \hat{\mathbf{n}}(\mathbf{x}) = q^P(\mathbf{x}, t) \quad (4.16b)$$

with $\hat{\mathbf{n}}(\mathbf{x})$ being the unit outward normal defined earlier. This minimization problem will result in a non-linear equation in terms of Lagrange multiplier for the hydrodynamic constraint:

$$\sum_{i \in M^-(\mathbf{x})} w_i (\mathbf{e}_i \cdot \hat{\mathbf{n}}(\mathbf{x})) \exp[-1 - \gamma \mathbf{e}_i \cdot \hat{\mathbf{n}}(\mathbf{x})] = q^P(\mathbf{x}, t) - \sum_{j \notin M^-(\mathbf{x})} (\mathbf{e}_j \cdot \hat{\mathbf{n}}(\mathbf{x})) f_j(\mathbf{x}, t) \quad (4.17)$$

where γ is the Lagrange multiplier. Once the value of γ is known, the populations can be found using the following relation:

$$f_i(\mathbf{x}, t) = w_i \exp[-1 - \gamma \mathbf{e}_i \cdot \hat{\mathbf{n}}(\mathbf{x})] \quad i \in M^-(\mathbf{x}) \quad (4.18)$$

which guarantees non-negative values for f_i . In the case of one-dimensional lattice models (e.g. the $D1Q2$ lattice) and the $D2Q4$ or $D2Q5$ models, this method reduces to the conventional bounce-back method. But, in general this method is different than bounce-back or specular reflection methods.

Through this method of enforcing boundary conditions, which is based on maximization of entropy, we ensure monotonic increase in entropy. The physical interpretation of this method is that the system in Ω is connected to systems in thermodynamic equilibrium. The adjacent systems connected to Ω through Γ^D and Γ^N are in different states of thermodynamic equilibrium. Minimization of the function \mathcal{H} ensures that the equilibrium condition for particles near the boundary is respected. The constraints in equations (4.14a) and (4.16a) are the macroscopic hydrodynamic conditions of the system at the respective points of the domain.

TABLE 1. Numerical results for LBM: In this table, numerical values for discretization parameters and the calculated error at time-level $t = 0.25$ are shown.

Case	h	Δt	$\mathcal{E}(t = 0.25)$
1	4×10^{-2}	3.3×10^{-3}	2.5×10^{-3}
2	2×10^{-2}	8.2×10^{-4}	6.2×10^{-4}
3	10^{-2}	2.1×10^{-4}	1.4×10^{-4}
4	5×10^{-3}	5.2×10^{-5}	1.7×10^{-5}

4.1.2. *A numerical example.* We now assess the accuracy of the proposed methods for boundary conditions under LBM. Consider the domain $\Omega = (0, 1) \times (0, 1)$, with the diffusion coefficient $D = \frac{4}{5\pi^2}$ and advection velocity being $\mathbf{v} = \mathbf{0}$. The source term is also zero throughout the domain. The initial concentration is taken as:

$$u_0(x, y) = \sin(\pi y) \cos(\pi x/2) \quad (4.19)$$

and the boundary conditions are

$$-D \text{grad}[u] \cdot \hat{\mathbf{n}} = 0 \quad \text{on } \Gamma^N \quad (4.20a)$$

$$u = 0 \quad \text{on } \Gamma^D \quad (4.20b)$$

where $\Gamma^N = \{0\} \times (0, 1)$ and $\Gamma^D = \partial\Omega - \Gamma^N$. We will employ the $D2Q9$ lattice model with grid spacing of h . The time-step will be chosen according to equation (4.9) to avoid negative values for discrete distributions. This problem is solved using several choices of discretization parameters as given in Table 1. We will use the following definition for calculation of error:

$$\mathcal{E}(t) = \max_i \{|u(\mathbf{x}_i, t) - u_{\text{exact}}(\mathbf{x}_i, t)|\} \quad (4.21)$$

where $u(\mathbf{x}_i, t)$ is the computed numerical value at i -th node and time-level t . The exact solution is denoted by u_{exact} . Numerical results from LBM with the proposed methods for boundary conditions are shown in figure 3. The variation of error with respect to the cell-size has been documented in Table 1 and figure 4, which show a second-order convergence.

4.1.3. *Comparison with other methods.* Consider the domain $\Omega = (0, 1) \times (0, 1)$ with zero-flux boundary conditions enforced on $\partial\Omega$. The initial condition is taken as:

$$u_0(\mathbf{x}) = \begin{cases} 1 & \mathbf{x} \in [a, b] \times [a, b] \\ 0 & \text{otherwise} \end{cases} \quad (4.22)$$

where we take $a = 0.4$ and $b = 0.6$. The diffusion coefficient is $D = 10^{-2}$ and the advection velocity is zero. The $D2Q9$ lattice model is used. Figure 5 shows the numerical result from the lattice Boltzmann method, along with the proposed methods for enforcing boundary conditions. The bound given by equation (4.9) for cell-size and time-step is respected. Hence, all discrete populations, and consequently, concentration at all nodes are non-negative. The change in the Boltzmann \mathcal{H} function is monotonic, which means that the \mathcal{H} -theorem is satisfied.

Note that a zero-flux boundary (or any other macroscopic boundary condition) can lead to various interpretations in the context of kinetic theory. For instance, a rigid and impermeable wall can lead to a zero-flux condition. Also, zero-flux can mean that there is a bath of particles at a Maxwell-Boltzmann equilibrium state with background velocity $\mathbf{v} = \mathbf{0}$. These interpretations are all valid in their own right. One needs to account for more physical details and choose the

right method for enforcing those conditions. To show the difference in the numerical results due to different treatment of boundaries under lattice Boltzmann method, the given numerical example is solved using bounce-back and specular reflection methods [Yu et al., 2003; Ziegler, 1993]. The difference in the solution is shown in figure 6. This difference should not be taken as a drawback of lattice Boltzmann method. It is in fact one of the advantages of kinetics-based methods over continuum-based methods. Extra information on the nature of interaction of particles with the boundary can be included in the numerical model. A continuum-based method may not be able to account for such details.

5. AN OVERLAPPING DOMAIN DECOMPOSITION METHOD

Domain decomposition methods are powerful methods for obtaining numerical solutions for partial differential equations [Quarteroni and Valli, 1999; Toselli and Widlund, 2005]. These methods are particularly effective in a parallel computing setting. The basic idea is to split the computational domain into an arbitrary number of subdomains and seek the numerical solution in different subdomains separately. These subdomains can be *overlapping* or *non-overlapping*. In a non-overlapping domain decomposition scheme, one needs to account for an interface equation to enforce compatibility of numerical solutions near the interface between subdomains. Two of the more popular methods for constructing interface compatibility conditions are Lagrange multiplier framework, Steklov-Poincaré framework [Quarteroni and Valli, 1999]. Introduction of such an interface condition may lead to higher complexity in the algorithm design but is also shown to give accurate numerical solutions. Overlapping domain decomposition do not require addition of a new interface constraint equation. In the proposed hybrid coupling method, we shall employ the overlapping domain decomposition approach. We now describe the iterative Schwartz method for numerical solution of a partial differential equation in an overlapping domain decomposition scheme.

Consider a domain Ω with boundary $\Gamma = \partial\Omega$. Consider the following equation defined on this domain:

$$\mathcal{L}[u] = f \quad \text{in } \Omega \quad (5.1a)$$

$$u = u^p \quad \text{on } \Gamma \quad (5.1b)$$

For simplicity, we assume that the boundary condition is purely Dirichlet, and employ two overlapping subdomains Ω_1 and Ω_2 (i.e., $\Omega_1 \cap \Omega_2 \neq \emptyset$ and $\Omega_1 \cup \Omega_2 = \Omega$). The governing partial differential equations in each subdomain will be as follows

$$\left\{ \begin{array}{ll} \mathcal{L}[u_1] = f_1 & \text{in } \Omega_1 \\ u_1 = u_2 & \text{on } \Gamma_1 \cap \Omega_2 \\ u_1 = u^p & \text{on } \Gamma_1 \cap \Gamma \end{array} \right\}, \quad \left\{ \begin{array}{ll} \mathcal{L}[u_2] = f_2 & \text{in } \Omega_2 \\ u_2 = u_1 & \text{on } \Gamma_2 \cap \Omega_1 \\ u_2 = u^p & \text{on } \Gamma_2 \cap \Gamma \end{array} \right\} \quad (5.2)$$

where the subindex is used to show the restriction of that quantity to the respective subdomain. The numerical solution to the system given in (5.2) can be found as

$$\left\{ \begin{array}{ll} \tilde{\mathcal{L}}[u_1^k] = f_1 & \text{in } \Omega_1 \\ u_1^k = u_2^{k-1} & \text{on } \Gamma_1 \cap \Omega_2 \\ u_1^k = u^p & \text{on } \Gamma_1 \cap \Gamma \end{array} \right\}, \quad \left\{ \begin{array}{ll} \tilde{\mathcal{L}}[u_2^{k+1}] = f_2 & \text{in } \Omega_2 \\ u_2^{k+1} = u_1^k & \text{on } \Gamma_2 \cap \Omega_1 \\ u_2^{k+1} = u^p & \text{on } \Gamma_2 \cap \Gamma \end{array} \right\} \quad (5.3)$$

where $\tilde{\mathcal{L}}$ is the discrete differential operator and super-indices $k-1$, k and $k+1$ are used to show consecutive iterations. The numerical solution in one subdomain, from the previous iteration, is

used to determine the Dirichlet condition on the boundary of other subdomain. This approach can be extended to the case where more than two subdomains are involved.

The advantages of overlapping domain decomposition methods compared to non-overlapping methods are simpler algorithm design, increased flexibility in choice of numerical solver in different subdomains, and easy incorporation of non-matching grids and multi-time-stepping. In the following section, we will further scrutinize the methods for projecting data from a coarse mesh to a fine grid, and vice versa.

5.1. Transfer of information across non-matching grids. Typically, the grid-size for a coarse-scale simulation is much larger than the grid-size for a fine-scale simulation. Under lattice Boltzmann method, small cell-size can help accounting for complex spatial features of the computational domain in a fine-scale simulation. Upscaled (averaged) models for flow and transport in porous media such as Darcy’s model do not need any such details of the pore structure, hence, the computational mesh for numerical solution of these models can be coarse. Under the proposed hybrid coupling method and the domain decomposition schemes introduced above, interaction among different subdomains occurs through the interface between any two subdomains. Transfer of information, consequently, needs to be done between non-matching grids that are disparate in size. This issue has been an active area of study in recent years. For instance, in simulation of fluid-structure interaction problems, traction at the interface of fluid and solid needs to be interpolated between non-matching grids [de Boer et al., 2007; Jaiman et al., 2006; Jiao and Heath, 2004]. In the context of overlapping domain decomposition schemes, numerical methods for flow and transport simulation on overlapping grids in [Chesshire and Henshaw, 1990; Henshaw and Schwendeman, 2003] and a study of stability of interpolation at the interface of subdomains in [Olsson and Petersson, 1996] can be mentioned. However, in this paper, since we intend to use different numerical methods in different subdomains (i.e., FEM or LBM), the interpolation for concentration is not alike. Our approach to transfer the values of concentration at the interface and across non-matching grids is described next.

Consider a two-dimensional domain and let $\tilde{\mathbf{x}}$ be the coordinates of a cell lying on the boundary of a subdomain of LBM discretization. Then, the values of the concentration at this point can be approximated via the finite element interpolation on the element that contains the point $\tilde{\mathbf{x}}$. To approximate concentration at a point $\tilde{\mathbf{x}}'$ that lies on the boundary of the subdomain with FEM discretization, one needs to locate the surrounding cells (of the LBM solution). Hence, the point $\tilde{\mathbf{x}}'$ is inside the square patch with the surrounding LBM nodes at the corners. Concentration at this finite element node can be approximated using the values of concentration at the surrounding points of the square patch. For instance, one can use a four-node quadrilateral finite element interpolation (figure 7 provides a pictorial description). Obviously, three-dimensional cases can be handled similarly, however, the choice of interpolation function can be more varied (e.g., one can use interpolation functions over hexagonal or tetrahedral elements identified with surrounding LBM nodes).

To demonstrate this technique, consider the following function defined over domain $\Omega = (0, 1) \times (0, 1)$:

$$g(x, y) = \sin(2\pi x) \sin(2\pi y) \tag{5.4}$$

TABLE 2. Transfer of information across non-matching grids: The numerical result for transfer of information from coarse grid to fine grid is given. The error is $\mathcal{O}(h^2)$, as expected.

Case	h	h'	\mathcal{E}_{\max}
1	10^{-1}	10^{-2}	9.55×10^{-2}
2	4.0×10^{-2}	10^{-2}	1.57×10^{-2}
3	2.0×10^{-2}	10^{-2}	3.94×10^{-3}

TABLE 3. Transfer of information across non-matching grids: In this table, numerical values for transferring information from fine grid to coarse grid is presented. The error in the values of the coarse-grid approximation behaves as $\mathcal{O}(h')$.

Case	h	h'	\mathcal{E}_{\max}
1	4.0×10^{-2}	2.0×10^{-2}	1.13×10^{-1}
2	4.0×10^{-2}	10^{-2}	5.75×10^{-2}
3	4.0×10^{-2}	5.0×10^{-3}	2.90×10^{-2}

The coarse grid size will be denoted by h (linear three-node triangular elements used) and the fine grid size is shown by h' . The maximum error in the domain is denoted by \mathcal{E}_{\max} and is defined by:

$$\mathcal{E}_{\max} = \max_{(x,y)} |g(x,y) - g(x,y)| \quad (5.5)$$

where (x,y) is a point on grid and $g(x,y)$ is the approximation of function g on a computational grid (either coarse or fine). Numerical results for transferring information across non-matching grids is given in Tables 2 and 3. From Table 2, we can conclude that the accuracy on the fine grid changes as $\mathcal{O}(h^2)$, which is expected, as it complies with the convergence rate of finite element approximation [Babuška and Suri, 1987]. However, the error on the coarse grid, with information transferred to it from the fine domain, is $\mathcal{O}(h')$. Figures 8 and 9 show some demonstrative numerical results and outline the process given above. From this numerical experiment we conclude that, a bottleneck in convergence of the proposed coupling method can be the accuracy of fine to coarse grid information transfer.

6. A NEW HYBRID MULTI-TIME-STEP COUPLING

In this section, we shall present a robust coupling method that allows hybrid modeling to be able to couple pore- and continuum-scale subdomains with disparate time-scales for solute transport in porous media. The spatial domain of interest Ω is partitioned into overlapping subdomains. The subdomains where *fine-scale* features of the solution are sought are denoted by Ω_f . Subdomains in which *coarse-scale* features are solved for are shown by Ω_c . Figure 10 provides a pictorial description of this partitioning scheme. In this paper, we will employ a finite element discretization in subdomain Ω_c . This finite element method is applied to the equation (3.2). The fine-scale features in subdomain Ω_f are solved for using the lattice Boltzmann method, which solves the Boltzmann's transport equation in equation (4.1) in the mentioned region. Compatibility of the solutions is enforced using a Dirichlet condition at $\Gamma_{f \rightarrow c}$ and $\Gamma_{c \rightarrow f}$. The time- and space-continuous partial differential equations

in each subdomain, along with their respective boundary conditions, are as follows:

$$\text{in } \Omega_c : \begin{cases} \partial u / \partial t + \text{div} [\mathbf{v}u - \mathbf{D}\text{grad}[u]] = s & (\mathbf{x}, t) \in \Omega_c \times \mathcal{I} \\ u(\mathbf{x}, t = 0) = u_0(\mathbf{x}) & \mathbf{x} \in \Omega_c \\ u(\mathbf{x}, t) = u^p(\mathbf{x}, t) & (\mathbf{x}, t) \in \Gamma^D \times \mathcal{I} \\ (\mathbf{v}u - \mathbf{D}\text{grad}[u]) \cdot \widehat{\mathbf{n}}(\mathbf{x}) = q^p(\mathbf{x}, t) & (\mathbf{x}, t) \in \Gamma^N \times \mathcal{I} \\ \text{coupling condition: } u(\mathbf{x}, t) = \tilde{u}_{f \rightarrow c}(\mathbf{x}, t) & (\mathbf{x}, t) \in \Gamma_{f \rightarrow c} \times \mathcal{I} \end{cases} \quad (6.1a)$$

$$\text{in } \Omega_f : \begin{cases} \partial f / \partial t + \mathbf{v} \cdot \text{grad}[f] = (f^{\text{eq}} - f) / \lambda & (\mathbf{x}, \boldsymbol{\zeta}, t) \in \Omega_f \times \mathbb{R}^n \times \mathcal{I} \\ f(\mathbf{x}, \boldsymbol{\zeta}, t = 0) = f^{\text{eq}}(\mathbf{x}, \boldsymbol{\zeta}, t = 0; u_0(\mathbf{x}), \mathbf{v}) & (\mathbf{x}, \boldsymbol{\zeta}) \in \Omega_f \times \mathbb{R}^n \\ \int f d\boldsymbol{\zeta} = u^p(\mathbf{x}, t) & (\mathbf{x}, t) \in \Gamma^D \times \mathcal{I} \\ (\int f \boldsymbol{\zeta} d\boldsymbol{\zeta}) \cdot \widehat{\mathbf{n}}(\mathbf{x}) = q^p(\mathbf{x}, t) & (\mathbf{x}, t) \in \Gamma^N \times \mathcal{I} \\ \text{coupling condition: } \int f d\boldsymbol{\zeta} = \tilde{u}_{c \rightarrow f}(\mathbf{x}, t) & (\mathbf{x}, t) \in \Gamma_{c \rightarrow f} \times \mathcal{I} \end{cases} \quad (6.1b)$$

This set of equations provides a basis to employ numerical methods of different origins in the same computational domain. The advection-diffusion equation is rooted in the continuum theory. The Boltzmann's equation however, is based on the kinetic theory. Using equation (6.1), one can solve for physical features at different temporal and spatial scales (macroscopic vs. mesoscopic), in a single computational framework. In the following, we will provide the temporal and spatial discretization of equation (6.1).

6.1. Space and time discretization.

6.1.1. *Coarse-scale problem.* The coarse-scale problem is defined by equation (3.2), over domain Ω_c in Figure 10. We will use the semi-discrete methodology [Zienkiewicz and Taylor, 1977], which gives the following time-continuous equation for the coarse-scale problem

$$\mathbf{M}\dot{\mathbf{u}} + \mathbf{K}\mathbf{u} = \mathbf{s} \quad (6.2)$$

where \mathbf{M} is the capacity matrix, \mathbf{K} is the transport matrix and \mathbf{u} is the nodal concentration. The superposed dot denotes the time derivative. The discretized right-hand-side of the finite element weak formulation is shown by \mathbf{s} . For time discretization, we will use the following notation

$$\mathbf{t}^{(n)} = n\Delta t_c, \quad \mathbf{u}(\mathbf{t}^{(n)}) \approx \mathbf{d}^{(n)}, \quad \dot{\mathbf{u}}(\mathbf{t}^{(n)}) \approx \mathbf{v}^{(n)} \quad (6.3)$$

where Δt_c is the time-step used for integrating the coarse-scale problem. Using the trapezoidal method for time integration yields the following system of equations

$$\mathbf{M}\mathbf{v}^{(n+1)} + \mathbf{K}\mathbf{d}^{(n+1)} = \mathbf{s}^{(n+1)} \quad (6.4a)$$

$$\mathbf{d}^{(n+1)} = \mathbf{d}^{(n)} + \Delta t_c(1 - \vartheta)\mathbf{v}^{(n)} + \Delta t_c\vartheta\mathbf{v}^{(n+1)} \quad (6.4b)$$

where $\vartheta \in [0, 1]$ is the time-integration parameter [Wood, 1990]. In this paper, we will use $\vartheta = 1/2$, which gives a second-order accurate and unconditionally stable time-integrator (the midpoint rule). Once the value of flux $\tilde{u}_{c \rightarrow f}$ is known, the values for nodal concentrations $\mathbf{d}^{(n+1)}$ and the rate variable $\mathbf{v}^{(n+1)}$ can be found. In the following section we will briefly overview the discretization of the fine-scale problem.

6.1.2. *Fine-scale problem.* Our objective is to solve for the distribution of particles in the phase space defined by $\Omega_f \times \mathbb{R}^n$. This goal can be achieved by solving the Boltzmann equation (4.1) numerically. The lattice Boltzmann method, introduced in Section 4, can provide relevant numerical results for simulation of the advection-diffusion process.

Consider a uniform grid, with the spacing between the cells equal to h_f , defined over the domain Ω_f . We will denote the time-step for the fine-scale problem by Δt_f , and the ratio $\eta = \Delta t_c / \Delta t_f$. The

procedure for updating the discrete populations over a time-step is the same as what was outlined earlier in Section 4.1. In the following section, we will describe the new computational framework in detail and point out the transfer of data from fine-scale to coarse-scale domain.

6.2. The proposed hybrid computational framework. Before providing a step-by-step procedure for a numerical simulation using the proposed framework, we need to introduce a set of tools that will be useful. These tools will enable multi-time-step integration and information transfer across non-matching grids. The details are as below:

- (i) **Initializing the discrete unknowns:** In Ω_c we utilize a finite element discretization. The nodal concentrations \mathbf{d} can be simply initialized according to $u_0(\mathbf{x})$. In Ω_f however, we assume that for the given initial concentration, the discrete populations f_i are given as

$$f_i(\mathbf{x}, t = 0) = f_i^{\text{eq}}(\mathbf{x}, t = 0; u_0(\mathbf{x})) \quad (6.5)$$

Other methods for initializing the discrete populations can also be considered.

- (ii) **Information transfer across the interface:** To identify values of prescribed concentration on interfaces $\Gamma_{f \rightarrow c}$ and $\Gamma_{c \rightarrow f}$, we need to approximate the concentration at nodes lying on these boundaries. Figure 11 is an illustrative example of lattice and finite elements at the boundary of each subdomain. We will denote the coordinates of the point j , numbered in figure 11, as (x_j, y_j) and the concentration at that node as u_i . For given concentrations at nodes 1 to 4, the concentration at node 5, which belongs to a finite element in Ω_c , can be approximated as follows:

$$u_5 \approx u_1(1 - \gamma_x)(1 - \gamma_y) + u_2\gamma_x(1 - \gamma_y) + u_3\gamma_x\gamma_y + u_4(1 - \gamma_x)\gamma_y \quad (6.6)$$

where $\gamma_x = (x_5 - x_1)/h_f$ and $\gamma_y = (y_5 - y_1)/h_f$. This method is obviously synonymous to approximation via a four-node quadrilateral element with its vertices lying on nodes 1 to 4. To transfer information from Ω_c to Ω_f , for instance at node number 1, one can use the finite element approximation in the element that includes the coordinates of node 1 (element i shown in figure 11). This value will serve as a Dirichlet-type condition on $\Gamma_{c \rightarrow f}$ and can be enforced using equation 4.14a. Three-dimensional cases can be handled similarly.

- (iii) **Multi-time-step integration:** The solution in Ω_c advances in time with a time-step of Δt_c . This time-step is typically much larger than the time-step needed for fine-scale problem in subdomain Ω_f . However, to perform time-integration in Ω_f , we need to know the concentration on $\Gamma_{c \rightarrow f}$, which can only be determined by the numerical values in Ω_c . To approximate the concentration on $\Gamma_{c \rightarrow f}$ at intermediate time-level j , between t and $t + \Delta t_c$, we will use the following interpolation in time:

$$u_c(\mathbf{x}, t + \frac{j}{\eta} \Delta t_c) \approx \left(\frac{j}{\eta}\right) u_c(\mathbf{x}, t + \Delta t_c) + \left(1 - \frac{j}{\eta}\right) u_c(\mathbf{x}, t) \quad \mathbf{x} \in \Gamma_{c \rightarrow f} \quad (6.7)$$

where u_c is the concentration in subdomain Ω_c . Here, we have assumed that the rate of change in concentration remains constant in a time-step Δt_c . This value for $u_c(\mathbf{x}, t + \frac{j}{\eta} \Delta t_c)$ will be enforced as a Dirichlet condition on the solution in Ω_f .

- (iv) **Sub-iterations at each time-step:** In order to ensure convergence of the proposed algorithm, one needs to transfer information between the subdomains iteratively. Compatibility of the numerical solutions from the pore and fine-scale problems at the overlap region $\Omega_f \cap \Omega_c$ has a vital role in accuracy of the numerical solution in the entire domain Ω . Figure 12 illustrates one iteration in a time-step Δt_c . The solution of the coarse-scale problem advances by Δt_c in

step 1. Using the updated values of solution in Ω_c , boundary conditions onto subdomain Ω_f at intermediate time-levels is determined. The solution of the fine-scale domain advances by time-step Δt_f successively. The new numerical values are then used to find the concentrations on boundary $\Gamma_{f \rightarrow c}$, which is used to update the solution in the coarse-scale domain in the next iteration. This procedure is repeated an arbitrary number of times in order to satisfy accuracy requirements defined by the user.

Given the tools described above, one can implement the proposed coupling method in a systematic manner. A step-by-step procedure is given in Algorithm 1. In the following section, we will provide numerical examples to showcase the performance of this framework.

Algorithm 1 Hybrid multi-time-step coupling framework: Outline of the algorithm for proposed framework.

```

1: Initialize  $\mathbf{u}$  in  $\Omega_c$  and  $f_i$  in  $\Omega_f$  for  $t = 0$ .
2: Set  $t \leftarrow 0$ 
3: while  $t < T$  do
4:   Set  $t \leftarrow t + \Delta t$ 
5:   Set Iter  $\leftarrow 0$ .
6:   while Iter  $\leq$  MaxIter do
7:     Set Iter  $\leftarrow$  Iter + 1.
8:     Find  $\tilde{u}_{f \rightarrow c}$  defined on  $\Gamma_{f \rightarrow c}$ .
9:     Advance the solution in  $\Omega_c$  by  $\Delta t_c$ .
10:    Find  $\tilde{u}_{c \rightarrow f}$  defined on  $\Gamma_{c \rightarrow f}$  at time-levels  $t - \Delta t_c$  and  $t$ .
11:    Set  $j \leftarrow 0$ 
12:    while  $j \leq \eta$  do
13:      Set  $j \leftarrow j + 1$ 
14:      Advance the solution in  $\Omega_f$  by  $\Delta t_f$  to find  $f_i(\mathbf{x}, t + j\Delta t_f)$  (stream and collide).
15:      Impose Dirichlet boundary condition on  $\Gamma_{c \rightarrow f}$  with
          
$$\tilde{u}_{c \rightarrow f}(\mathbf{x}, t + j\Delta t_f) = (1 - j/\eta)\tilde{u}_{c \rightarrow f}(\mathbf{x}, t - \Delta t_c) + (j/\eta)\tilde{u}_{c \rightarrow f}(\mathbf{x}, t)$$

16:    end while
17:    From the new numerical values in  $\Omega_f$  find  $\tilde{u}_{f \rightarrow c}$ .
18:  end while
19: end while

```

6.3. The case of many subdomains. Thus far, the proposed coupling algorithm is presented for the case of only two subdomains, a coarse-scale subdomain Ω_c and a fine-scale domain Ω_f . However, in practical applications decomposition into multiple subdomains may be required. In this section, we will present the proposed coupling method for cases where there are multiple coarse and fine-scale subdomains.

Suppose that the domain $\Omega \subset \mathbb{R}^n$ is partitioned into coarse and fine-scale subdomains, given as follows:

$$\Omega = \underbrace{\left(\bigcup_{i=1}^{N_c} \Omega_{c,i} \right)}_{\text{coarse-scale subdomains}} \cup \underbrace{\left(\bigcup_{j=1}^{N_f} \Omega_{f,j} \right)}_{\text{fine-scale subdomains}} \quad (6.8)$$

where all coarse and fine-scale subdomains are overlapping. The number of coarse-scale subdomains is shown by N_c and N_f is the number of fine-scale subdomains. Each subdomain $\Omega_{f,j}$ (for $j = 1, \dots, N_f$) is a fine-scale subdomain and will be integrated using the lattice Boltzmann method with grid size $h_{f,j}$ and time-step Δt_j . Coarse-scale subdomains $\Omega_{c,i}$ (for $i = 1, \dots, N_c$) are solved using the finite element method with mesh-size $h_{c,i}$ and $\Delta t_{c,i}$. The details regarding multi-time-stepping and transferring data from coarse-scale grid to fine-scale grid (and vice versa) remains the same as before. Since discretization parameters for coarse-scale domains are much larger than the ones used in the fine-scale subdomains, the solution in coarse-scale domains advances first, then the updated values near the interface of coarse-scale/fine-scale subdomains are used for multi-time-step integration. Obviously, even coarse-scale subdomains can be integrated with different time-steps. Multi-time-step integration for the coarse-scale subdomains can be done in the same spirit as for the coarse-scale subdomains presented earlier. However, an alternative approach would be to use the method presented in [Karimi and Nakshatrala, 2015a] to solve the coarse-scale subdomains (that share an interface), and then use the updated solution to transfer to fine-scale domains. We will not follow this procedure here, but it can be explored in future research endeavors. We will denote the system time-step, the same definition used in [Karimi and Nakshatrala, 2015a], by Δt . The proposed coupling framework for the case of multiple subdomains is given in Algorithm 2.

Algorithm 2 Hybrid multi-time-step coupling framework for many subdomains: The algorithmic procedure for the proposed framework is outlined.

```

1: Set  $t \leftarrow 0$ 
2: while  $t + \Delta t < T$  do
3:   for Iter = 1, ... do
4:     for  $i = 1, \dots, N_c$  do
5:       Advance the solution in subdomain  $\Omega_{c,i}$  by one system time-step, subject to boundary
       values from the solutions from previous iteration.
6:     end for
7:     for  $j = 1, \dots, N_f$  do
8:       Advance the solution in subdomain  $\Omega_{f,j}$  by one system time-step, subject to boundary
       values approximated by equation (6.7).
9:     end for
10:   end for
11: end while

```

7. REPRESENTATIVE NUMERICAL RESULTS

In this section, we will apply the proposed coupling algorithm to one- and two-dimensional problems. The performance of the new method with respect to discretization parameters will be studied. Computer implementation is done using NumPy [van der Walt et al., 2011] and FEniCS [Logg et al., 2012] software packages.

7.1. Advection and diffusion of one-dimensional Gaussian hill. Consider $\Omega = (0, 1)$ with zero-flux condition imposed on both ends. The initial concentration is given as

$$u_0(x) = \frac{\phi}{\sqrt{2\pi\sigma_0^2}} e^{-(x-x_0)^2/2\sigma_0^2} \quad (7.1)$$

where $\phi = 10^{-1}$ and $\sigma_0 = 10^{-2}$. The initial location of the tip of the Gaussian hill is at \mathbf{x}_0 and is set to be 3×10^{-1} . The advection velocity in the entire domain is taken to be $v = 1$ and the diffusion coefficient is $D = 10^{-2}$. The source term is taken to be zero and the time-interval of interest is $T = 4 \times 10^{-2}$. We will use the proposed hybrid coupling method to numerically solve this problem. We will use the finite element method with the Galerkin formulation in Ω_c and the lattice Boltzmann method in Ω_f . To showcase the performance of the proposed method, we will use the following definition for error (error in ∞ -norm)

$$\mathcal{E}(t) = \max_{i=1, \dots, N} |u(\mathbf{x}_i, t) - u_{\text{exact}}(\mathbf{x}_i, t)| \quad (7.2)$$

where N is the number of nodes for numerical solution, $u(\mathbf{x}, t)$ is the approximate solution at point \mathbf{x}_i and time t . The exact solution is represented by u_{exact} . Following the definition given in (7.2), the error in Ω_c and Ω_f will be denoted by \mathcal{E}_c and \mathcal{E}_f respectively. We will denote the length of the overlap region $\Omega_f \cap \Omega_c$ by L_{overlap} . The domain partitioning is as follows

$$\Omega_c = \left(0, \frac{1}{2} + \frac{L_{\text{overlap}}}{2}\right), \quad \Omega_f = \left(\frac{1}{2} - \frac{L_{\text{overlap}}}{2}, 1\right) \quad (7.3)$$

We will employ two-node linear finite elements of equal lengths h_c to discretize Ω_c . The time-step is set to be $\Delta t_c = h_c^2/2D$. Subdomain Ω_f is discretized using a uniform grid with spacing h_f and a time-step of $\Delta t_f = h_f^2/2D$. The *D1Q2* lattice model will be used in Ω_f . The number of sub-iterations in each time-step is shown by `MaxIter`.

Figure 13 shows a comparison between the numerical solution from the hybrid coupling framework and the exact solution. The concentration profile is shown when the front is passing through the overlap region and afterwards. In both cases, the numerical solution is in accordance with the exact solution.

The numerical experiments discussed here show that the proposed hybrid coupling framework gives an accurate solution to the advection-diffusion equation and is indeed a converging scheme (see figures 14 and 15). From these numerical experiments, we conclude that the convergence of the numerical solution under the proposed framework is $\mathcal{O}(h)$. In the following, the effect of discretization in coarse and fine-scale subdomains, effect of length of overlap region and the number of sub-iterations on the accuracy of the numerical solution are described.

- (1) Discretization in fine-scale domain: Our numerical experiments indicate that for a given discretization in the coarse-scale domain (i.e., h_c and Δt_c), refinement of parameters h_f and Δt_f improves the overall accuracy of numerical solution. The results presented in Table 4 show that the mentioned refinement reduces the error in both fine-scale and coarse-scale subdomains.
- (2) Discretization in coarse-scale domain: Considering the numerical results presented in Table 5, one can conclude that for a given discretization in fine-scale domain (i.e., h_f and Δt_f), refinement of respective parameters in the coarse-scale domain does not necessarily improve accuracy. This behavior can be attributed to the fact that the lower accuracy in the fine-scale domain (due to use of lattice Boltzmann method), results in a less accurate estimation of the concentration on $\Gamma_{f \rightarrow c}$. Hence, the numerical solution in the coarse-scale region converges to a solution other than the exact solution.
- (3) Length of overlap region: For a given discretization in subdomains Ω_f and Ω_c , increase in the length of the overlap region results in reduction of overall accuracy. This conclusion can be drawn from the numerical experiments presented in Table 6. However, if the grid-size and time-step in both subdomains change simultaneously, convergence rate of the numerical solution to

TABLE 4. Advection and diffusion of one-dimensional Gaussian hill: In this table, the accuracy of the numerical solution using the proposed coupling framework is shown. Here, only cell size and time-step in the fine-scale domain are refined. Note that despite the refinement in the fine-scale domain only, the accuracy of the solution in the entire computational domain is improving.

h_c	Δt_c	h_f	Δt_f	η	L_{overlap}	MaxIter	$\mathcal{E}_c(\text{T})$	$\mathcal{E}_f(\text{T})$
10^{-2}	5.00×10^{-3}	5.00×10^{-3}	1.25×10^{-3}	4	10^{-1}	4	3.67×10^{-3}	1.70×10^{-2}
10^{-2}	5.00×10^{-3}	2.50×10^{-3}	3.13×10^{-4}	16	10^{-1}	4	1.94×10^{-3}	7.42×10^{-3}
10^{-2}	5.00×10^{-3}	1.25×10^{-3}	7.81×10^{-5}	64	10^{-1}	4	1.02×10^{-3}	3.48×10^{-3}
10^{-2}	5.00×10^{-3}	6.25×10^{-4}	1.95×10^{-5}	256	10^{-1}	4	5.50×10^{-4}	1.80×10^{-3}

the exact solution may slow down. Following the numerical results given in Tables 7, 8 and 9, as well as figures 15, 16 and 17 shows that convergence under simultaneous refinement in both subdomains has an inverse relation to the length of the overlap region.

- (4) Number of sub-iterations in each time-step: In the numerical experiments performed, increasing the maximum number of sub-iterations to values greater than 4 did not result in a significant improvement in accuracy. However, compatibility, especially near the overlap region, can be improved by increasing the number of sub-iterations.
- (5) Order of interpolation in the coarse-scale subdomain: Figure 18 shows the point-wise error in the coarse-scale subdomain, for different orders of interpolation in finite elements and under multi-time-stepping. For different cases, the error in the fine-scale subdomain remains largely unchanged from one case to another. Error in the coarse-scale subdomain decreases by increasing the order of interpolation, however, the error near the overlap region remains unchanged. The figure the error accumulates near the overlapping region under both multi-time-stepping and under single time-step in all the subdomains.

These observations regarding the effect of number of sub-iterations and length of the overlap region are in accordance with the theory of overlapping domain decomposition methods [Chang et al., 2015; Nataf and Nier, 1997]. It seems that, generally, decrease in the size of the overlap region reduces the rate of convergence and the error decreases proportional to the inverse of square root of number of sub-iterations. One key observation from these numerical experiments is that majority of error in the numerical solution accumulates near the overlap region. This error can be much higher than the error in the rest of the domain and refinement in either of the subdomains may not improve it. Hence, a topic for future research can be designing efficient methods for removing the accumulated error in the overlap region under the proposed coupling framework.

Here, we showed that one can use highly disparate mesh-size and time-steps in different subdomains. Furthermore, we showed that to improve accuracy throughout the computational domain, grid refinement in the fine-scale domain is sufficient. We also demonstrated that mesh refinement only in the coarse-scale domain may not lead to a more accurate numerical solution.

7.2. Simulation of fast bimolecular reaction using multiple subdomains. This example will be used to demonstrate the application of the proposed hybrid framework for bimolecular fast reactions and its ability to handle multiple subdomains. To this end, we simulate the evolution of

TABLE 5. Advection and diffusion of one-dimensional Gaussian hill: In this table, performance of the proposed method for numerical solution of the one-dimensional problem is shown. In this case, element size and time-step refinement are done only in the coarse-scale domain. The discretization parameters in the fine-scale domain remain unchanged in the fine-scale domain. It can be observed that refinement, merely in the coarse-scale domain, has adverse effect on the accuracy of numerical solution. This experiment shows that the numerical method with the slowest convergence has the dominant role in overall accuracy.

h_c	Δt_c	h_f	Δt_f	η	L_{overlap}	MaxIter	$\mathcal{E}_c(\text{T})$	$\mathcal{E}_f(\text{T})$
10^{-2}	5.00×10^{-3}	1.25×10^{-3}	7.81×10^{-5}	64	10^{-1}	4	1.02×10^{-3}	3.48×10^{-3}
5.00×10^{-3}	1.25×10^{-3}	1.25×10^{-3}	7.81×10^{-5}	16	10^{-1}	4	1.65×10^{-3}	3.71×10^{-3}
2.50×10^{-3}	3.13×10^{-4}	1.25×10^{-3}	7.81×10^{-5}	4	10^{-1}	4	2.01×10^{-3}	3.74×10^{-3}
1.25×10^{-3}	7.81×10^{-5}	1.25×10^{-3}	7.81×10^{-5}	1	10^{-1}	4	2.22×10^{-3}	3.74×10^{-3}

TABLE 6. Advection and diffusion of one-dimensional Gaussian hill: This numerical experiment indicates that increasing the length of the overlapping region could have adverse effect on the accuracy of the numerical solution.

h_c	Δt_c	h_f	Δt_f	η	L_{overlap}	MaxIter	$\mathcal{E}_c(\text{T})$	$\mathcal{E}_f(\text{T})$
10^{-2}	5.00×10^{-3}	1.25×10^{-3}	7.81×10^{-5}	64	2.00×10^{-2}	4	5.78×10^{-4}	3.08×10^{-3}
10^{-2}	5.00×10^{-3}	1.25×10^{-3}	7.81×10^{-5}	64	4.00×10^{-2}	4	5.85×10^{-4}	3.43×10^{-3}
10^{-2}	5.00×10^{-3}	1.25×10^{-3}	7.81×10^{-5}	64	8.00×10^{-2}	4	8.63×10^{-4}	3.47×10^{-3}
10^{-2}	5.00×10^{-3}	1.25×10^{-3}	7.81×10^{-5}	64	10^{-1}	4	1.02×10^{-3}	3.48×10^{-3}

TABLE 7. Advection and diffusion of one-dimensional Gaussian hill: In this table, values of discretization parameters and errors in each subdomain are provided. In all the cases, $\eta = 4$ and $L_{\text{overlap}} = 4 \times 10^{-2}$. The number of sub-iterations in each time-step is 10.

h_c	Δt_c	h_f	Δt_f	$\mathcal{E}_c(\text{T})$	$\mathcal{E}_f(\text{T})$
1.00×10^{-2}	5.00×10^{-3}	5.00×10^{-3}	1.25×10^{-3}	2.55×10^{-3}	1.64×10^{-2}
5.00×10^{-3}	1.25×10^{-3}	2.50×10^{-3}	3.13×10^{-4}	2.22×10^{-3}	7.54×10^{-3}
2.50×10^{-3}	3.13×10^{-4}	1.25×10^{-3}	7.81×10^{-5}	1.40×10^{-3}	3.70×10^{-3}
1.25×10^{-3}	7.81×10^{-5}	6.25×10^{-4}	1.95×10^{-5}	7.79×10^{-4}	1.85×10^{-3}
6.25×10^{-4}	1.95×10^{-5}	3.13×10^{-4}	4.88×10^{-6}	4.11×10^{-4}	1.75×10^{-3}
3.13×10^{-4}	4.88×10^{-6}	1.56×10^{-4}	1.22×10^{-6}	2.11×10^{-4}	1.73×10^{-3}

the concentrations of the participating chemical species in the following bimolecular reaction:



where n_A , n_B and n_C are the stoichiometry coefficients. Here, we have chosen $n_A = 1$, $n_B = 2$ and $n_C = 1$. The computational domain $\Omega = (0, 1)$ is partitioned into the following two coarse-scale and

TABLE 8. Advection and diffusion of one-dimensional Gaussian hill: Values for the discretization parameters and errors in fine and coarse-scale subdomains are given. In all cases, $\eta = 4$, $L_{\text{overlap}} = 10^{-2}$ and the number of sub-iterations is 10.

h_c	Δt_c	h_f	Δt_f	$\mathcal{E}_c(\text{T})$	$\mathcal{E}_f(\text{T})$
5.00×10^{-3}	1.25×10^{-2}	2.50×10^{-3}	3.13×10^{-4}	3.32×10^{-3}	4.09×10^{-3}
2.50×10^{-3}	3.13×10^{-4}	1.25×10^{-3}	7.81×10^{-5}	2.07×10^{-3}	2.12×10^{-3}
1.25×10^{-3}	7.81×10^{-5}	6.25×10^{-4}	1.95×10^{-5}	1.14×10^{-3}	1.72×10^{-3}
6.25×10^{-4}	1.95×10^{-5}	3.13×10^{-4}	4.88×10^{-6}	6.00×10^{-4}	1.72×10^{-3}

TABLE 9. Advection and diffusion of one-dimensional Gaussian hill: Discretization and errors in fine-scale and coarse-scale domains are given in this table. The number of sub-iterations in each time-step is 10. In all the cases, $\eta = 4$ and $L_{\text{overlap}} = 10^{-1}$.

h_c	Δt_c	h_f	Δt_f	$\mathcal{E}_c(\text{T})$	$\mathcal{E}_f(\text{T})$
1.00×10^{-2}	5.00×10^{-3}	5.00×10^{-3}	1.25×10^{-3}	3.67×10^{-3}	1.70×10^{-2}
5.00×10^{-3}	1.25×10^{-3}	2.50×10^{-3}	3.13×10^{-4}	3.16×10^{-3}	7.67×10^{-3}
2.50×10^{-3}	3.13×10^{-4}	1.25×10^{-3}	7.81×10^{-5}	2.01×10^{-3}	3.74×10^{-3}
1.25×10^{-3}	7.81×10^{-5}	6.25×10^{-4}	1.95×10^{-5}	1.13×10^{-3}	1.86×10^{-3}
6.25×10^{-4}	1.95×10^{-5}	3.13×10^{-4}	4.88×10^{-6}	6.02×10^{-4}	1.73×10^{-3}

one fine-scale subdomains:

$$\Omega_{c,1} = (0, 0.40), \quad \Omega_f = (0.39, 0.61) \quad \text{and} \quad \Omega_{c,2} = (0.6, 1.0)$$

The time-interval of interest is $\text{T} = 0.5$. The coefficient of diffusion is $\text{D} = 10^{-2}$ and the advection velocity is zero throughout the domain. We will enforce zero-flux boundary conditions at $x = 0$ and $x = 1$. The initial values for each of the species is as follows:

$$u_{0,i}(x) = \frac{\phi_{0,i}}{\sqrt{2\pi\sigma^2}} \exp\left[-(x - x_{0,i})^2/2\sigma^2\right] \quad i = \text{A, B, C} \quad (7.5)$$

where $\sigma = 0.1$, $\phi_{0,\text{A}} = 0.1$, $x_{0,\text{A}} = 0.3$, $\phi_{0,\text{B}} = 0.05$ and $x_{0,\text{B}} = 0.7$. The initial concentration of the species C is zero in the entire domain. To solve the problem numerically, it is convenient to introduce the following invariants:

$$\alpha = u_{\text{A}} + \frac{n_{\text{A}}}{n_{\text{C}}} u_{\text{C}} \quad \text{and} \quad \beta = u_{\text{B}} + \frac{n_{\text{B}}}{n_{\text{C}}} u_{\text{C}} \quad (7.6)$$

where u_{A} , u_{B} and u_{C} are the concentrations of the chemical species A, B and C, respectively. Once numerical values for α and β are found, the concentrations of the participating chemical species can be calculated as follows:

$$u_{\text{A}} = \max\left\{\alpha - \frac{n_{\text{A}}}{n_{\text{B}}}\beta, 0\right\} \quad (7.7a)$$

$$u_{\text{B}} = \frac{n_{\text{B}}}{n_{\text{A}}} \max\left\{-\alpha + \frac{n_{\text{A}}}{n_{\text{B}}}\beta, 0\right\} \quad (7.7b)$$

$$u_{\text{C}} = \frac{n_{\text{C}}}{n_{\text{A}}} (\alpha - u_{\text{A}}) \quad (7.7c)$$

Subdomains $\Omega_{c,1}$ and $\Omega_{c,2}$ are discretized using the finite element method, with a mesh size of $h_{c,1} = h_{c,2} = 10^{-2}$ and time-step of $\Delta t_{c,1} = \Delta t_{c,2} = 5 \times 10^{-3}$. Subdomain Ω_f is solved using the

lattice Boltzmann method with cell size of $h_f = 10^{-3}$ and time-step $\Delta t_f = 2 \times 10^{-5}$. The number of sub-iterations at each time-level is set to 10.

Numerical results at various time-levels are presented in figures 19–21, which show the concentrations of all the participating chemical species from the coarse-scale subdomains (which are denoted by $u_{c,1}$ and $u_{c,2}$) and the fine-scale subdomain (which is denoted by u_f). As evident from these figures, the numerical solution is compatible near and in the overlap region, and the proposed hybrid framework has performed well.

7.3. Advection and diffusion in a homogeneous medium. Consider $\Omega = (0, 2) \times (0, 1/4)$ with $\Gamma^D = \{0\} \times [0, 1/4]$ and $\Gamma^N = \partial\Omega - \Gamma^D$ corresponding to the following boundary conditions

$$u^p(\mathbf{x}, t) = 1 \quad \mathbf{x} \in \Gamma^D, t \in \mathcal{I} \quad (7.8)$$

$$q^p(\mathbf{x}, t) = 0 \quad \mathbf{x} \in \Gamma^N, t \in \mathcal{I} \quad (7.9)$$

where $\mathcal{I} = (0, T]$ is the time interval of interest. The initial concentration in the entire domain is taken to be $u_0(\mathbf{x}) = 0$. The isotropic diffusion coefficient is $D = 5 \times 10^{-3}$. Here, we shall use the proposed framework to numerically solve this problem for different Péclet numbers. We will define the coarse-scale domain Ω_c and the fine-scale domain Ω_f as follows:

$$\Omega_c = \left(0, 1 + \frac{L_{\text{overlap}}}{2}\right) \times (0, 1/4), \quad \Omega_f = \left(0, 1 - \frac{L_{\text{overlap}}}{2}\right) \times (0, 1/4) \quad (7.10)$$

where we pick $L_{\text{overlap}} = 4/100$. The SUPG formulation (3.6) with linear three-node triangular elements will be used in Ω_c . Numerical solution in Ω_f will be sought for using lattice Boltzmann method with the $D2Q4$ lattice model. In figure 22 non-matching grid sized for finite element and lattice Boltzmann methods in the given domain is illustrated. We shall solve the problem for two different choices of advection velocity:

- (i) *Case 1:* Considering the uniform advection velocity of $v_x = 5 \times 10^{-2}$ and $v_y = 0$ over domain Ω , we find the Péclet number as $P = 20$. The element-size in the coarse-scale domain is $h_c \approx 7 \times 10^{-2}$, and the grid spacing for LBM is $h_f = 10^{-2}$. The time-steps in the coarse-scale and fine-scale subdomains are $\Delta t_c = 5.1 \times 10^{-1}$ and $\Delta t_f = 10^{-2}$ respectively. Note that the ratio between the coarse and fine time-steps is $\eta = 51$. The number of iterations is $\text{MaxIter} = 5$. The result is shown in figure 23. The numerical solution from FEM and LBM retained good compatibility while the concentration front passed through the subdomain interfaces. The coupling of the two methods did not result in any disruptions on the propagation of the chemical species in the domain.
- (ii) *Case 2:* Here, we will take $v_x = 5 \times 10^{-1}$ and $v_y = 0$. In this case the advection velocity is much higher than the previous case, hence, the Péclet number is $P = 200$. In this case, the gradient of concentration near the front is steep. We take $h_c \approx 2.5 \times 10^{-2}$, $h_f = 2 \times 10^{-3}$ in coarse and fine-scale subdomains respectively. The time-steps are $\Delta t_c = 10^{-1}$ and $\Delta t_f = 4 \times 10^{-4}$. The ratio between the time-steps is $\eta = 250$. Similar to the previous case, the number of sub-iterations is $\text{MaxIter} = 5$. The numerical results are shown in figure 24. One of the numerical difficulties that can occur in this case is the spurious oscillations in the concentration. It can be observed that the numerical solution in the coarse-scale domain experiences some of this oscillations (see figure 24(a)), however, it should be noted that this weak instability is not due to the hybrid coupling and is an artifact of the finite element formulation. With mesh refinement, these instabilities can be removed. Note that when the front is reaching the interface of the subdomains, some minor incompatibility between the numerical solution

of different subdomains in the overlap region is seen (see figure 24(b)). This incompatibility can be alleviated by increasing the number of sub-iterations in each time-step. As expected, once the front leaves the coarse-scale domain completely, no node-to-node oscillations remain. In figure 25, the numerical solution using smaller time-steps and mesh size is shown. The time-step in the coarse-scale domain is $\Delta t_c = 2 \times 10^{-2}$ and $\Delta t_f = 4 \times 10^{-4}$ in the fine-scale domain. The element-size in the coarse-scale subdomain is $h_c \approx 1.8 \times 10^{-2}$ and in the fine-scale subdomain is $h_f = 2 \times 10^{-3}$. The number of sub-iterations in each time-step is increased to 10. Hence, spurious oscillations and incompatibility in the overlap region (while the front is passing through the interface) are largely reduced.

In this numerical experiment we conclude that in order to capture interior/boundary layers more accurately, mere mesh or time-step refinement is not enough. One needs to increase the number of sub-iterations in each time-step.

7.4. Hybrid simulation of dissolution of calcium carbonate in porous media. Calcium carbonate CaCO_3 is a common chemical compound found in the subsurface. The dissolution of calcium carbonate is an important geochemical equilibrium reaction, which arises in a wide variety of subsurface applications [Drever, 1988]. The chemical reaction takes the following form:



For convenience, we shall use u_1 , u_2 and u_3 to denote the concentrations of CaCO_3 , Ca^{2+} and CO_3^{2-} , respectively. This chemical reaction is known to have a product solubility constant K_{sp} of about 3.36×10^{-9} at room temperature [Benjamin, 2002]. The product solubility for this chemical reaction can be written as:

$$K_{\text{sp}} = \frac{u_2 u_3}{u_1} \quad (7.12)$$

We introduce the following two reaction invariants:

$$\psi_1 = u_1 - u_2 \quad (7.13a)$$

$$\psi_2 = u_3 - u_2 \quad (7.13b)$$

It should be emphasized that ψ_1 and ψ_2 are not the concentrations of any real chemical species. These invariants are introduced to simplify the problem, as they decouple the governed equations and hence can be solved for separately; for example, see [Nakshatrala et al., 2013]. Once the values of ψ_1 and ψ_2 are found, the concentration of the species Ca^{2+} can be determined using the following relation:

$$u_2 = \frac{1}{2} \left(-(\psi_2 + K_{\text{sp}}) + \sqrt{(\psi_2 + K_{\text{sp}})^2 + 4K_{\text{sp}}\psi_1} \right) \quad (7.14)$$

which is obtained by solving equations (7.12)–(7.13) for u_2 . The values of u_1 and u_3 can then be determined using equations (7.13a)–(7.13b). Here, we are interested in determining the fate of the chemical species due to the chemical reaction and transport. We employ the LBM to simulate the transport problem at the pore-scale (fine-scale) and the FEM at the continuum-scale.

The computational domain is shown in figure 26 where in $L_x = 2$ and $L_y = 1$. The radius of the solid obstacles in Ω_f (the fine-scale problem) is taken as $r = 10^{-1}$. The length of the overlap region is set to $L_{\text{overlap}} = 10^{-1}$. Obviously, because of the geometry of Ω_f , a more detailed description of the flow is required. We used LBM with a *D2Q9* lattice model to solve the Navier-Stokes equations in the fine-scale subdomain Ω_f [Succi, 2001; Yu et al., 2003]. The prescribed components on the

inlet velocity on the boundary $x = 0$ are $v_x = 1$ and $v_y = 0$. The pressure on $\Gamma_{f \rightarrow c}$ is set to be zero and periodic boundary conditions are enforced on the boundaries located at $y = 0$ and $y = 1$ for $0 < x < (L_x + L_{\text{overlap}})/2$. The resulting velocity field is shown in figure 27 and will be used as the advection velocity for the fine-scale problem. In the overlap region, the average velocity in the x-direction is close to 1 and the average velocity in the y-direction is close to 0. Hence, the advection velocity in the coarse-scale domain is taken to be $v_x = 1$ and $v_y = 0$. The values of concentrations on the boundary of the domain are shown in figure 28 and the diffusion coefficient is taken to be $D = 10^{-1}$. For numerical simulation of the advection-diffusion problem, we will use $h_c = 5.0 \times 10^{-2}$ and $h_f = 4.0 \times 10^{-3}$. The time-steps are $\Delta t_c = 10^{-1}$ and $\Delta t_f = 4.0 \times 10^{-5}$ (the ratio between the time-steps is $\eta = 2500$). Furthermore, we will use the *D2Q9* lattice model in the fine-scale domain (solved using LBM). The non-matching grid near the overlap region is shown in figure 29. Obviously, one of the advantages of the proposed coupling algorithm is that fine-scale features (such as advection velocity within the pores) can be accounted for without a noticeable overhead in the computational cost. In this problem, fine-scale features are sought after only in Ω_f , and a coarse estimate in Ω_c is deemed enough.

The concentrations of the participating chemical species are shown in figures 30–32. The numerical simulation reveals that the concentrations of CaCO_3 and CO_3^{2-} inside the domain increase with time. However, the evolution of Ca^{2+} cations is completely different from that of the other two chemical species. At earlier time-levels, when the concentrations of CaCO_3 and CO_3^{2-} are low within the domain, Ca^{2+} has a more noticeable presence throughout the domain. At later time-levels, as a consequence of increasing concentration of CO_3^{2-} anions, Ca^{2+} disappears from much of the domain and gathers in the regions where the concentration of CO_3^{2-} is low. Figure 33 further corroborates this finding, in which the normalized total concentrations of chemical species are plotted against time. The total concentration in the entire domain, $\mathcal{C}_{\text{total}}$, is defined as

$$\mathcal{C}_{\text{total}}(t) = \int_{\Omega} u_i(\mathbf{x}, t) \, d\Omega, \quad i = 1, 2, 3 \quad (7.15)$$

The normalization for each chemical species is done with respect to the corresponding maximum in the time interval of interest. That is,

$$\max_t \mathcal{C}_{\text{total}}(t) \quad (7.16)$$

In this example, we have demonstrated how to use the proposed multi-time-step hybrid coupling framework for the analysis of geochemical processes by simultaneously incorporating both pore and continuum models. A detailed pore geometry and complex transport processes can be accounted for in the fine-scale domain, whereas a rough approximation can be sought in the coarse-scale domain.

8. CONCLUDING REMARKS

Simulation of transport of chemical species in porous media poses several challenges. These include disparate mathematical scales in space and time, not all the essential physical and chemical processes can be upscaled from the pore-scale to the meso-scale, high computational cost to solve realistic problem; just to name a few. In this paper, we have presented a computational framework that can make multi-scale simulation of transport in porous media feasible even for realistic problems. The framework allows to take into account the features and processes at the pore-scale and still be able to solve problems at the field-scale with manageable computational cost. The findings and advances made in this paper can be listed as follows:

- (i) **Simulation of advection and diffusion using LBM:** The lattice Boltzmann method for simulation of transport is outlined. A drawback of LBM in such simulations can be the possibility of discrete distributions attaining unphysical (negative) values. To rectify this issue, we presented a bound on discretization parameters under LBM that guarantees non-negativity of discrete populations. Furthermore, new methods for enforcing macroscopic boundary values, in the form of Neumann or Dirichlet conditions, on the numerical solution from the LBM are proposed. These methods are based on entropy principles and warrant non-negative values for discrete populations.
- (ii) **Information transfer across non-matching grids:** Methods for transferring information from one computational grid to another non-matching grid were documented. Accuracy of these methods with respect to grid size in different domains is also explored.
- (iii) **Governing equations for hybrid simulation:** Time and space continuous partial differential equations for coupled analysis are presented. These equations provide a precise mathematical framework for further developments in this area of research.
- (iv) **Hybrid coupling computational framework:** A numerical framework, based on domain decomposition, was presented that can employ different numerical methods (e.g., finite element method and lattice Boltzmann method) in different subdomains. This framework can account for pore-scale processes as well as continuum scale models. Also, disparate spatial and temporal discretization can be incorporated. Hence, the primary factor in choosing grid size and time-steps in each subdomain is the accuracy in that subdomain. The hybrid coupling framework poses no restriction on the discretization parameters in different subdomains. Furthermore, various chemical reaction dynamics among the present chemical species can be included using LBM and other approximations of the same phenomena in the finite element solver. In all of the numerical experiments, this framework was numerically stable and accurate. Interior layers can be captured accurately and typical weak instabilities in the solution can be suppressed using appropriate numerical techniques (such as stabilized finite element formulations) in those subdomains. We also demonstrated application of this framework in assessing the fate of chemical species in a sample geochemical reaction problem. As a courtesy of its domain decomposition basis, this framework provides the user with great flexibility in distributing the computational workload onto different processors and possibly in a heterogeneous GPU-CPU computing setup. For instance, the subdomains solved using the lattice Boltzmann method can be transferred to a GPU, while other subdomains where the finite element method is used can be solved for using a different processing environment. This computational framework can handle multiple subdomains using the multiplicative Schwartz methods.

We shall conclude the paper by outlining some possible future research directions.

- (R1) A good research endeavor can be towards a comprehensive mathematical analysis (i.e., stability, accuracy and convergence properties) of the proposed computational framework.
- (R2) One can implement the proposed computational framework in a combined GPU-CPU computing environment, and study the numerical performance of such an implementation.
- (R3) Substantial progress in development of hybrid methods can result from extension of the proposed computational framework to fully coupled thermal-flow-transport processes, including precipitation at the solid-fluid interface (in pore-scale) and application of such methods to simulation of viscous fingering and other physical instabilities.

References

- P. Albuquerque, D. Alemani, B. Chopard, and P. Leone. Coupling a lattice Boltzmann and a finite difference scheme. In *Computational Science-ICCS 2004*, pages 540–547. Springer, 2004.
- T. Arbogast, G. Pencheva, M. F. Wheeler, and I. Yotov. A multiscale mortar mixed finite element method. *Multiscale Modeling & Simulation*, 6(1):319–346, 2007.
- M. Astorino, F. Chouly, and A. Quarteroni. A time-parallel framework for coupling finite element and lattice Boltzmann methods. Research report, LMB - CMCS - MOX, 2014. URL <https://hal.archives-ouvertes.fr/hal-00746942>.
- M. Augustin, A. Caiazzo, A. Fiebach, J. Fuhrmann, V. John, A. Linke, and R. Umla. An assessment of discretizations for convection-dominated convection–diffusion equations. *Computer Methods in Applied Mechanics and Engineering*, 200(47):3395–3409, 2011.
- I. Babuška and M. Suri. The optimal convergence rate of the p-version of the finite element method. *SIAM Journal on Numerical Analysis*, 24(4):750–776, 1987.
- M. T. Balhoff, S. G. Thomas, and M. F. Wheeler. Mortar coupling and upscaling of pore-scale models. *Computational Geosciences*, 12(1):15–27, 2008.
- I. Battiato, D. M. Tartakovsky, A. M. Tartakovsky, and T. Scheibe. On breakdown of macroscopic models of mixing-controlled heterogeneous reactions in porous media. *Advances in Water Resources*, 32(11):1664–1673, 2009.
- I. Battiato, D. M. Tartakovsky, A. M. Tartakovsky, and T. D. Scheibe. Hybrid models of reactive transport in porous and fractured media. *Advances in Water Resources*, 34(9):1140–1150, 2011.
- S. Bekri, J. F. Thovert, and P. M. Adler. Dissolution of porous media. *Chemical Engineering Science*, 50(17):2765–2791, 1995.
- M. M. Benjamin. *Water Chemistry*. Waveland Press Inc., Long Grove, 2002.
- P. L. Bhatnagar, E. P. Gross, and M. Krook. A model for collision processes in gases. I. small amplitude processes in charged and neutral one-component systems. *Physical Review*, 94(3):511, 1954.
- T. Bridges and S. Reich. Multi-symplectic integrators: Numerical schemes for Hamiltonian PDEs that conserve symplecticity. *Physics Letters A*, 284(4):184–193, 2001.
- X. C. Cai and Y. Saad. Overlapping domain decomposition algorithms for general sparse matrices. *Numerical Linear Algebra with Applications*, 3(3):221–237, 1996.
- C. Cercignani. *The Boltzmann Equation and its Applications*. Springer, New York, 1988.
- C. Cercignani and M. Lampis. Kinetic models for gas-surface interactions. *Transport Theory and Statistical Physics*, 1(2):101–114, 1971.
- C. Cercignani, R. Illner, and M. Pulvirenti. *The Mathematical Theory of Dilute Gases*, volume 106. Springer Science & Business Media, New York, 2013.
- H. Chang, X. Tai, L. Wang, and D. Yang. Convergence rate of overlapping domain decomposition methods for the Rudin–Osher–Fatemi model based on a dual formulation. *SIAM Journal on Imaging Sciences*, 8(1):564–591, 2015.
- Q. Chen, X. Zhang, and J. Zhang. Improved treatments for general boundary conditions in the lattice Boltzmann method for convection-diffusion and heat transfer processes. *Physical Review E*, 88(3):033304, 2013.
- S. Chen and G. D. Doolen. Lattice Boltzmann method for fluid flows. *Annual Review of Fluid Mechanics*, 30(1):329–364, 1998.

- G. Chesshire and W. D. Henshaw. Composite overlapping meshes for the solution of partial differential equations. *Journal of Computational Physics*, 90(1):1–64, 1990.
- E. M. Constantinescu and A. Sandu. Extrapolated multirate methods for differential equations with multiple time scales. *Journal of Scientific Computing*, 56(1):28–44, 2013.
- A. de Boer, A. H. Van Zuijlen, and H. Bijl. Review of coupling methods for non-matching meshes. *Computer Methods in Applied Mechanics and Engineering*, 196(8):1515–1525, 2007.
- S. Dellacherie. Construction and analysis of lattice Boltzmann methods applied to a 1D convection-diffusion equation. *Acta Applicandae Mathematicae*, 131(1):69–140, 2014.
- J. I. Drever. *The Geochemistry of Natural Waters*. Prentice Hall, New Jersey, 1988.
- L. C. Evans. *Partial Differential Equations*. American Mathematical Society, Providence, Rhode Island, 1998.
- I. Fatt. The network model of porous media. *Petroleum Transactions*, 207:144–181, 1956.
- L. P. Franca, S. L. Frey, and T. J. R. Hughes. Stabilized finite element methods: I. application to the advective-diffusive model. *Computer Methods in Applied Mechanics and Engineering*, 95(2):253–276, 1992.
- C. M. Gramling, C. F. Harvey, and L. C. Meigs. Reactive transport in porous media: A comparison of model prediction with laboratory visualization. *Environmental Science & Technology*, 36(11):2508–2514, 2002.
- P. M. Gresho and R. L. Sani. *Incompressible Flow and the Finite Element Method: Advection-Diffusion*, volume 1. John Wiley & Sons, Inc., Chichester, UK, 2000.
- M. Günther, A. Kvaernø, and P. Rentrop. Multirate partitioned Runge-Kutta methods. *BIT Numerical Mathematics*, 41(3):504–514, 2001.
- I. W. Haslam, R. S. Crouch, and M. Seaïd. Coupled finite element–lattice Boltzmann analysis. *Computer Methods in Applied Mechanics and Engineering*, 197(51):4505–4511, 2008.
- X. He and L. Luo. Theory of the lattice Boltzmann method: From the Boltzmann equation to the lattice Boltzmann equation. *Physical Review E*, 56(6):6811, 1997.
- W. D. Henshaw and D. W. Schwendeman. An adaptive numerical scheme for high-speed reactive flow on overlapping grids. *Journal of Computational Physics*, 191(2):420–447, 2003.
- T. Y. Hou and X. H. Wu. A multiscale finite element method for elliptic problems in composite materials and porous media. *Journal of computational physics*, 134(1):169–189, 1997.
- T. J. R. Hughes, G. R. Feijóo, L. Mazzei, and J. Quincy. The variational multiscale method? a paradigm for computational mechanics. *Computer Methods in Applied Mechanics and Engineering*, 166(1):3–24, 1998.
- W. H. Hundsdorfer and J. G. Verwer. *Numerical Solution of Time-Dependent Advection-Diffusion-Reaction Equations*. Springer-Verlag, New York, USA, 2007.
- R. K. Jaiman, X. Jiao, P. H. Geubelle, and E. Loth. Conservative load transfer along curved fluid–solid interface with non-matching meshes. *Journal of Computational Physics*, 218(1):372–397, 2006.
- X. Jiao and M. T. Heath. Common-refinement-based data transfer between non-matching meshes in multiphysics simulations. *International Journal for Numerical Methods in Engineering*, 61(14):2402–2427, 2004.
- S. Karimi and K. B. Nakshatrala. On multi-time-step monolithic coupling algorithms for elastodynamics. *Journal of Computational Physics*, 273:671–705, 2014.

- S. Karimi and K. B. Nakshatrala. A monolithic multi-time-step computational framework for first-order transient systems with disparate scales. *Computer Methods in Applied Mechanics and Engineering*, 283:419–453, 2015a.
- S. Karimi and K. B. Nakshatrala. Do current lattice Boltzmann methods for diffusion and diffusion-type equations respect maximum principles and the non-negative constraint? *arXiv:1503.08360*, 2015b.
- I. V. Karlin, S. Ansumali, C. E. Frouzakis, and S. S. Chikatamarla. Elements of the lattice Boltzmann method i: Linear advection equation. *Communications in Computational Physics*, 1(4): 616–655, 2006.
- P. Lallemand and L. S. Luo. Theory of the lattice Boltzmann method: Dispersion, dissipation, isotropy, Galilean invariance, and stability. *Physical Review E*, 61(6):6546, 2000.
- B. Leimkuhler and S. Reich. *Simulating Hamiltonian Dynamics*. Cambridge University Press, Cambridge, U.K., 2004.
- A. Lew, J. E. Marsden, M. Ortiz, and M. West. Variational time integrators. *International Journal for Numerical Methods in Engineering*, 60(1):153–212, 2004.
- Y. Li, R. Shock, R. Zhang, and H. Chen. Numerical study of flow past an impulsively started cylinder by the lattice-Boltzmann method. *Journal of Fluid Mechanics*, 519:273–300, 2004.
- P. L. Lions. On the Schwarz alternating method. i. In *First International Symposium on Domain Decomposition Methods for Partial Differential Equations*, pages 1–42. Paris, France, 1988.
- A. Logg, K. Mardal, and G. Wells. *Automated Solution of Differential Equations by the Finite Element Method: The FEniCS Book*. Springer, Berlin Heidelberg, 2012.
- T. Mathew. *Domain Decomposition Methods for the Numerical Solution of Partial Differential Equations*. Springer, Berlin Heidelberg, 2008.
- Y. Mehmani and M. T. Balhoff. Bridging from pore to continuum: A hybrid mortar domain decomposition framework for subsurface flow and transport. *Multiscale Modeling & Simulation*, 12(2):667–693, 2014.
- J. M. Melenk and I. Babuška. The partition of unity finite element method: Basic theory and applications. *Computer Methods in Applied Mechanics and Engineering*, 139(1):289–314, 1996.
- J. J. Monaghan. Smoothed particle hydrodynamics. *Reports on Progress in Physics*, 68(8):1703, 2005.
- E. M. Murphy and T. R. Ginn. Modeling microbial processes in porous media. *Hydrogeology Journal*, 8(1):142–158, 2000.
- K. B. Nakshatrala, K. D. Hjelmstad, and D. A. Tortorelli. A FETI-based domain decomposition technique for time-dependent first-order systems based on a DAE approach. *International Journal for Numerical Methods in Engineering*, 75(12):1385–1415, 2008.
- K. B. Nakshatrala, M. K. Mudunuru, and A. J. Valocchi. A numerical framework for diffusion-controlled bimolecular-reactive systems to enforce maximum principles and the non-negative constraint. *Journal of Computational Physics*, 253:278–307, 2013.
- F. Nataf and F. Nier. Convergence rate of some domain decomposition methods for overlapping and nonoverlapping subdomains. *Numerische Mathematik*, 75(3):357–377, 1997.
- T. L. Van Noorden and I. S. Pop. A Stefan problem modeling crystal dissolution and precipitation. *IMA Journal of Applied Mathematics*, 73(2):393–411, 2008.
- F. Olsson and N. A. Petersson. Stability of interpolation on overlapping grids. *Computers and Fluids*, 25(6):583–605, 1996.

- A. Quarteroni and A. Valli. *Domain Decomposition Methods for Partial Differential Equations*. Oxford University Press, Oxford, 1999.
- T. D. Scheibe, E. M. Murphy, X. Chen, A. K. Rice, K. C. Carroll, B. J. Palmer, A. M. Tartakovsky, I. Battiato, and B. D. Wood. An analysis platform for multiscale hydrogeologic modeling with emphasis on hybrid multiscale methods. *Groundwater*, 53(1):38–56, 2015.
- M. Shapiro and H. Brenner. Taylor dispersion of chemically reactive species: irreversible first-order reactions in bulk and on boundaries. *Chemical Engineering Science*, 41(6):1417–1433, 1986.
- P. A. Skordos. Initial and boundary conditions for the lattice Boltzmann method. *Physical Review E*, 48(6):4823, 1993.
- S. Succi. *The Lattice Boltzmann Equation*. Oxford University Press, Oxford, 2001.
- T. Sun, Y. Mehmani, and M. T. Balhoff. Hybrid multiscale modeling through direct substitution of pore-scale models into near-well reservoir simulators. *Energy & Fuels*, 26(9):5828–5836, 2012.
- Y. Tang, A. J. Valocchi, and C. J. Werth. A hybrid pore-scale and continuum-scale model for solute diffusion, reaction, and biofilm development in porous media. *Water Resources Research*, 51(3):1846–1859, 2015.
- A. M. Tartakovsky, D. M. Tartakovsky, T. D. Scheibe, and P. Meakin. Hybrid simulations of reaction-diffusion systems in porous media. *SIAM Journal on Scientific Computing*, 30(6):2799–2816, 2008.
- A. Toselli and O. Widlund. *Domain Decomposition Methods: Algorithms and Theory*, volume 3. Springer, Heidelberg, 2005.
- S. van der Walt, S. C. Colbert, and G. Varoquaux. The NumPy array: A structure for efficient numerical computation. *Computing in Science & Engineering*, 13:22–30, 2011.
- B. I. Wohlmuth. A mortar finite element method using dual spaces for the Lagrange multiplier. *SIAM Journal on Numerical Analysis*, 38(3):989–1012, 2000.
- B. D. Wood, K. Radakovich, and F. Golfier. Effective reaction at a fluid–solid interface: applications to biotransformation in porous media. *Advances in Water Resources*, 30(6):1630–1647, 2007.
- W. L. Wood. *Practical Time-stepping Schemes*. Clarendon Press, Oxford, 1990.
- W. Xian and A. Takayuki. Multi-GPU performance of incompressible flow computation by lattice Boltzmann method on GPU cluster. *Parallel Computing*, 37(9):521–535, 2011.
- D. Yu, R. Mei, L. Luo, and W. Shyy. Viscous flow computations with the method of lattice Boltzmann equation. *Progress in Aerospace Sciences*, 39(5):329–367, 2003.
- D. P. Ziegler. Boundary conditions for lattice Boltzmann simulations. *Journal of Statistical Physics*, 71:1171–1177, 1993.
- O. C. Zienkiewicz and R. L. Taylor. *The Finite Element Method*. McGraw-Hill, London, 1977.
- Q. Zou and X. He. On pressure and velocity boundary conditions for the lattice Boltzmann BGK model. *Physics of Fluids*, 9(6):1591–1598, 1997.

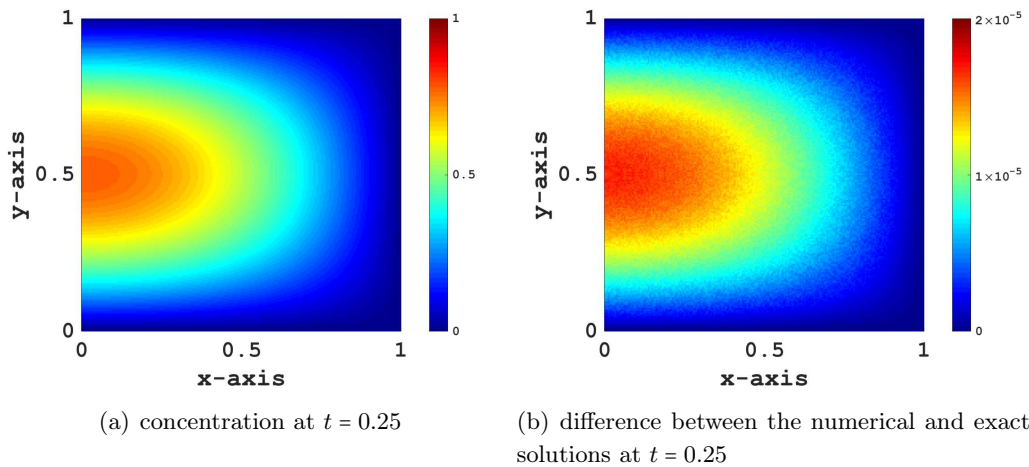


FIGURE 3. Numerical results for LBM: Concentration and error in concentration are shown over the computational domain. LBM along with the new method for enforcing boundary conditions provide accurate numerical solutions, as illustrated in this example. These results correspond to Case 4 in Table 1.

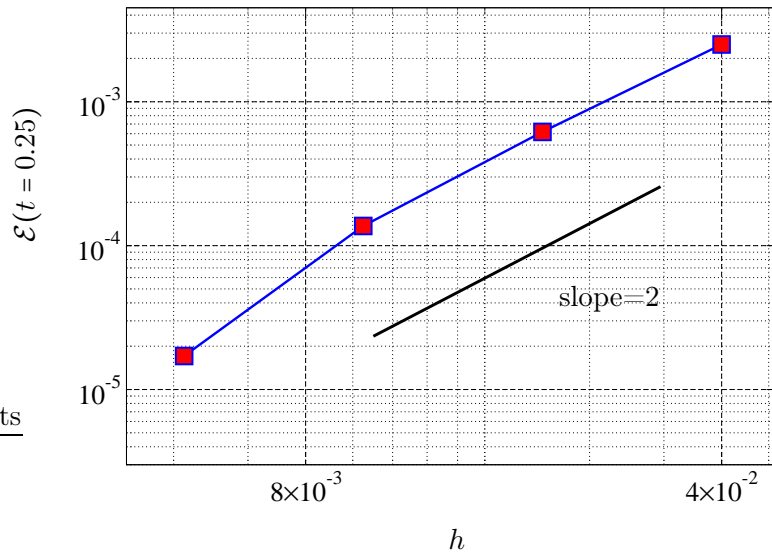
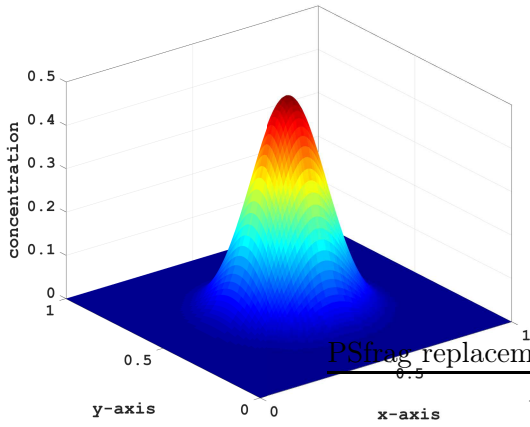
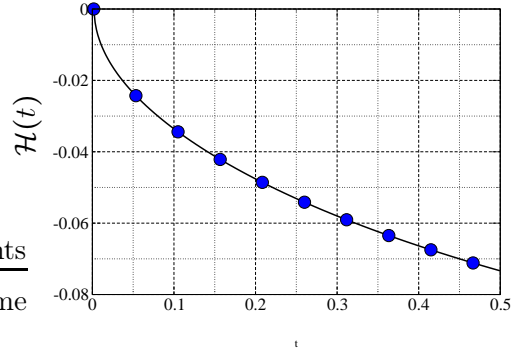


FIGURE 4. Numerical results for LBM: In this figure, the error in the numerical solution is shown against the lattice cell size. With the proposed method for the boundary conditions, second-order convergence of LBM is obtained.

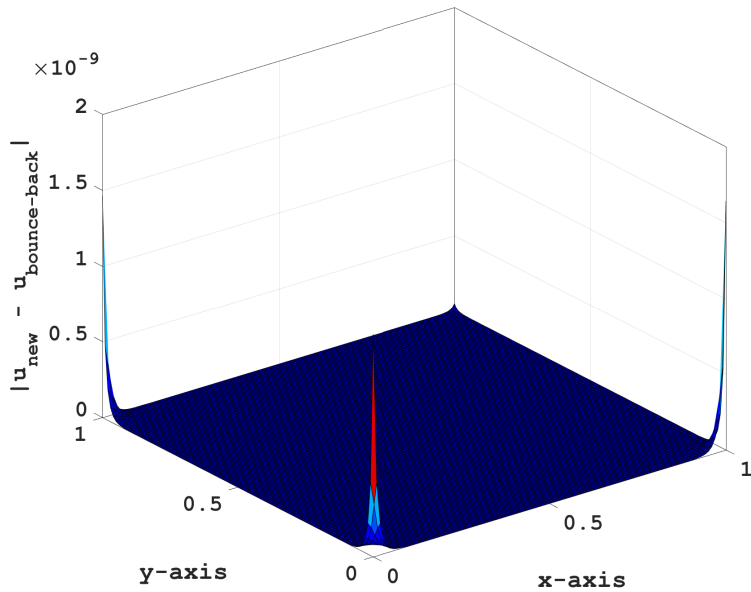


(a) Concentration at $t = 0.5$

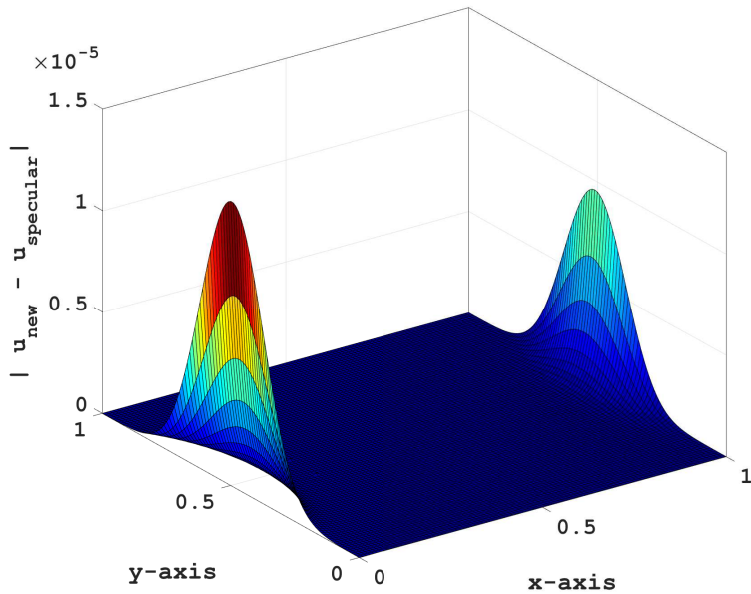


(b) Boltzmann's \mathcal{H} function

FIGURE 5. Numerical results for LBM: This figure presents sample numerical results under the lattice Boltzmann method with the new boundary conditions. Figure (a) shows the concentration at time $t = 0.5$, which is non-negative throughout the domain. In figure (b), the value of the Boltzmann's \mathcal{H} function is plotted against time. Clearly, the value of \mathcal{H} is decreasing monotonically with time.



(a) proposed boundary condition vs. bounce-back method



(b) proposed boundary condition vs. specular reflection method

FIGURE 6. Numerical results for LBM: In this figure, the difference between the numerical solution due to different treatment of zero-flux boundary is shown. This implies that a macroscopic boundary condition (i.e., Dirichlet or Neumann) can be interpreted in different ways in the context of lattice Boltzmann scheme.

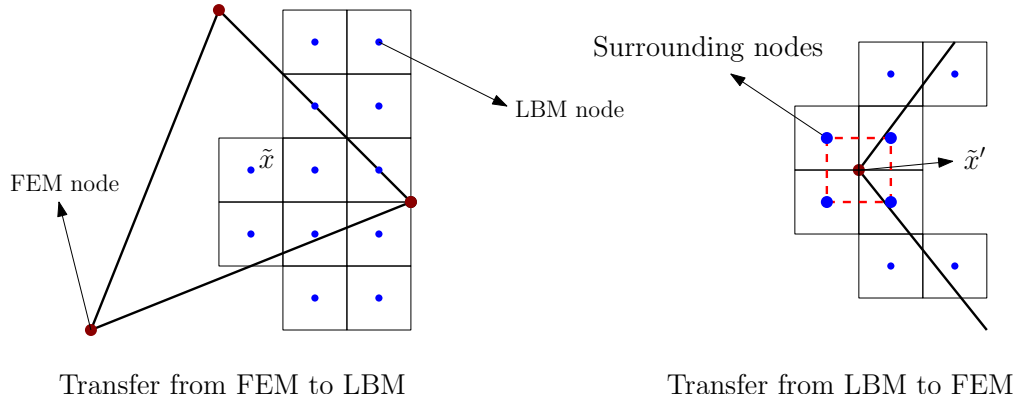
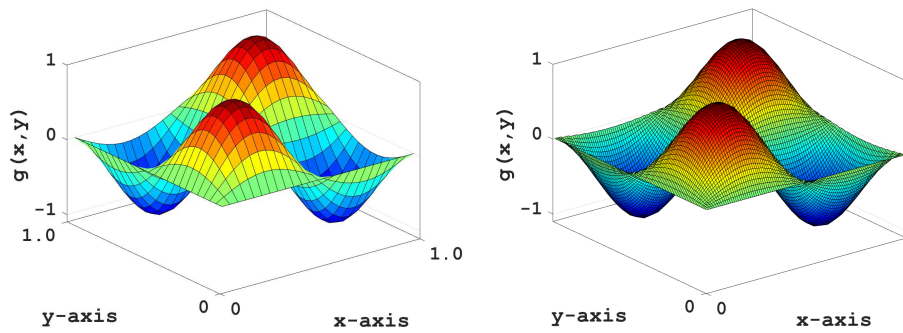
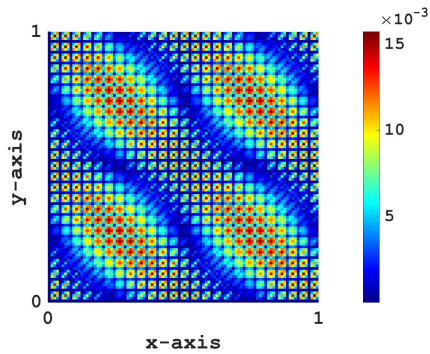


FIGURE 7. Transfer of information across non-matching grids: A pictorial description for interpolation across non-matching grids is provided. In transferring information from FEM to LBM, one only needs to use the FEM interpolation already in use to approximate concentration at the lattice node. In transferring from LBM to FEM however, the surrounding lattice nodes need to be located to form a patch.

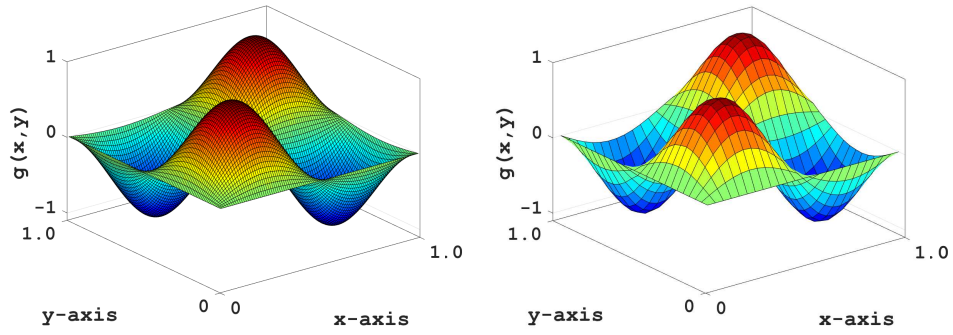


(a) approximation of $g(x,y)$ on coarse grid: $g(x,y) \rightarrow g_c(x,y)$ (b) transfer of information from coarse grid to fine grid: $g_c(x,y) \rightarrow g_f(x,y)$

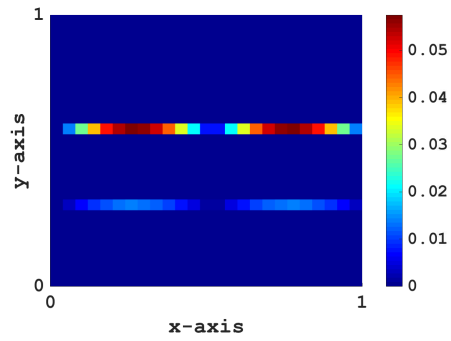


(c) error on the fine grid: $|g_f(x,y) - g(x,y)|$

FIGURE 8. Transfer of information across non-matching grids: The function $g(x,y)$ is first approximated on a coarse grid. Then, it is mapped onto a fine grid. The error in the final approximation (on fine grid) is also shown. The data corresponds to Case 2 in Table 2.



(a) approximation of $g(x,y)$ on fine grid: (b) transfer of information from fine grid to coarse grid: $g_f(x,y) \rightarrow g_c(x,y)$



(c) error on coarse grid: $|g_c(x,y) - g(x,y)|$

FIGURE 9. Transfer of information across non-matching grids: The function $g(x,y)$ is first approximated on a fine grid. Then, it is mapped onto a coarse grid using the method described in figure 7. The error on the coarse grid is shown as well. The data corresponds to Case 2 in Table 3.

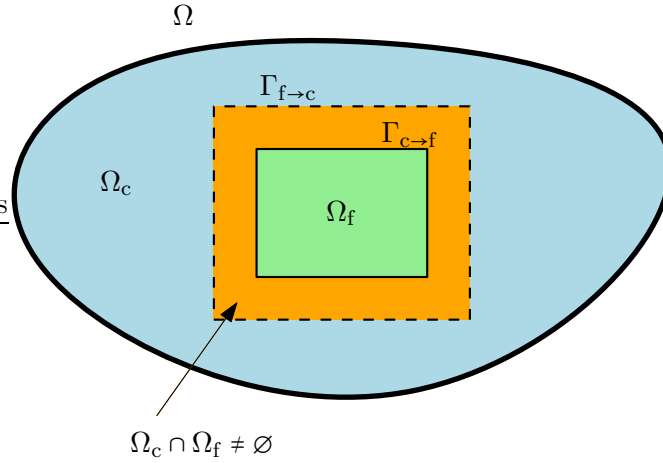


FIGURE 10. **Overlapping domain partitioning:** The proposed coupling method employs overlapping domain partitioning. This figure illustrates the decomposition of the computational domain Ω into the subdomains where coarse-scale and fine-scale features are sought after. These subdomains are denoted by Ω_c and Ω_f , respectively. The portions of the boundary of the mentioned subdomains where transfer of information occurs are denoted by $\Gamma_{f \rightarrow c}$ and $\Gamma_{c \rightarrow f}$. Obviously, $\Gamma_{f \rightarrow c} \subseteq \partial\Omega_c$ and $\Gamma_{c \rightarrow f} \subseteq \partial\Omega_f$. An attractive feature of this partitioning technique is that the grid sizes in subdomains Ω_c and Ω_f need not be conforming.

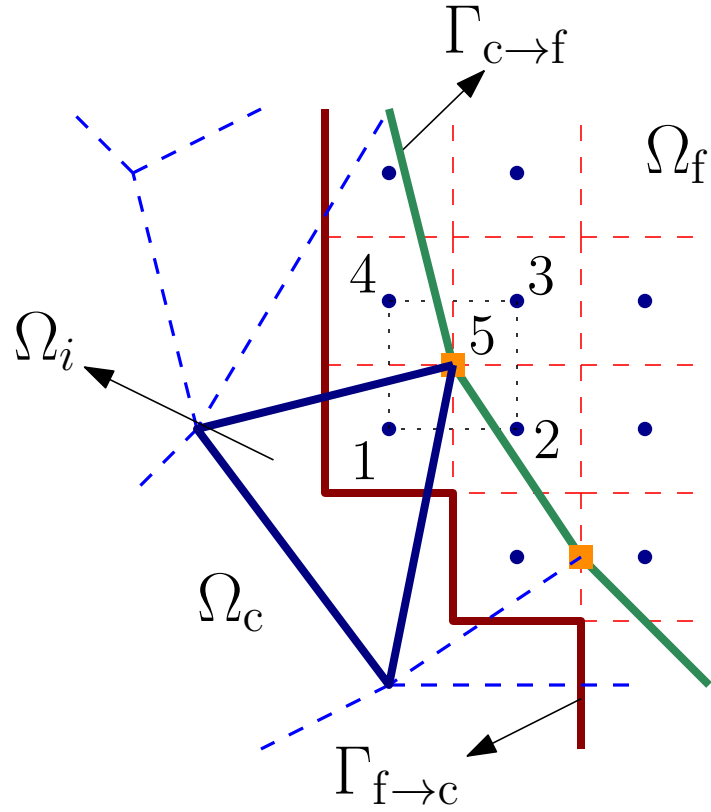


FIGURE 11. Information transfer across non-matching grids: In this figure, transfer of information at the interface of subdomains is depicted. The proposed coupling method allows non-conforming grids, which is a basic requirement of any multi-scale computational framework. Nodes 1 to 4 and 6 denote representative LBM cells and node 5 is a finite element node. The spatial domain inside i -th element is denoted by Ω_i , which is an arbitrary element near $\Gamma_{c \rightarrow f}$.

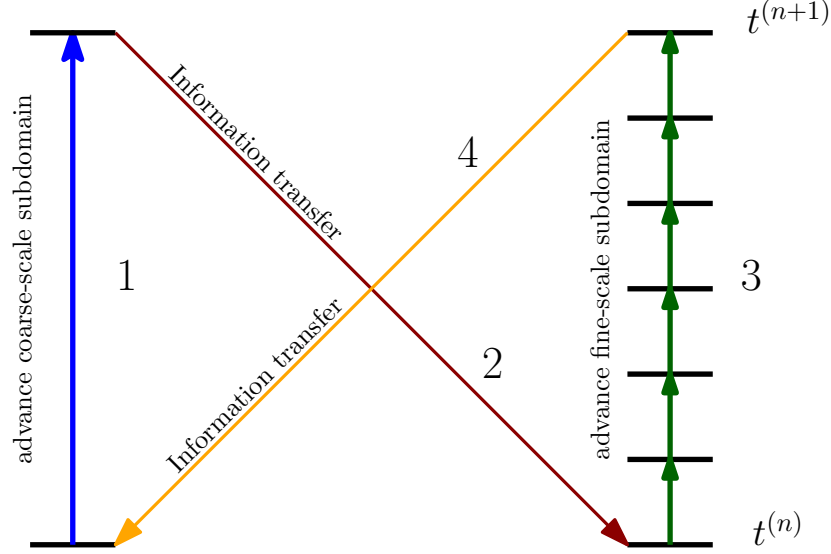


FIGURE 12. Proposed coupling method: In this figure, use of multiple time-steps for time-integration under the proposed coupling framework is demonstrated. In step 1, the solution in the coarse-scale domain advances in time by Δt_c . In step 2, interface information is transferred to the fine-scale domain, using the updated values from the coarse-scale domain. The solution in the fine-scale domain progresses in time in step 3. In step 4, updated solution in the fine-scale domain is used to alter the interface condition for the coarse-scale domain.

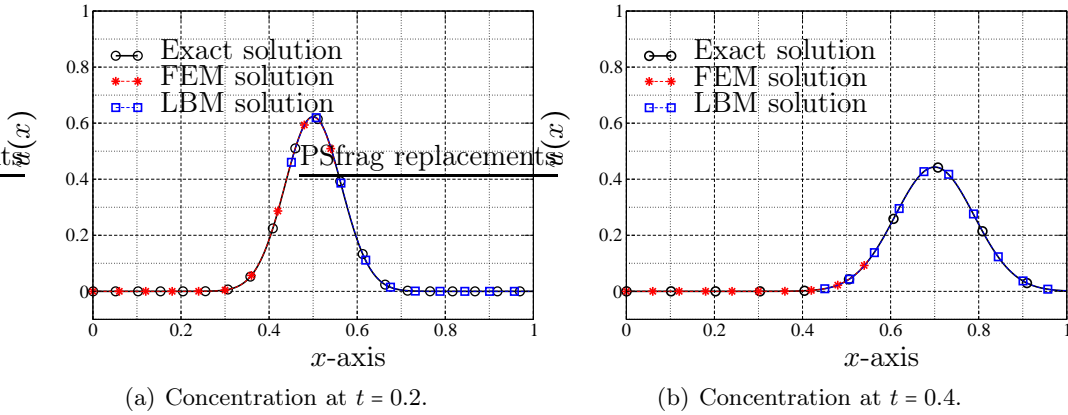


FIGURE 13. Advection and diffusion of one-dimensional Gaussian hill: This figure shows the exact and numerical concentration profiles at two different time-levels. At $t = 0.2$, the front passes through the overlap region. The numerical solution shows good agreement with the exact solution. We have taken $h_c = 10^{-2}$ and $\Delta t_c = 5 \times 10^{-3}$. In the fine-scale domain, $h_f = 1.25 \times 10^{-3}$ and $\Delta t_f = 7.81 \times 10^{-5}$. Length of the overlap region is $L_{\text{overlap}} = 0.1$.

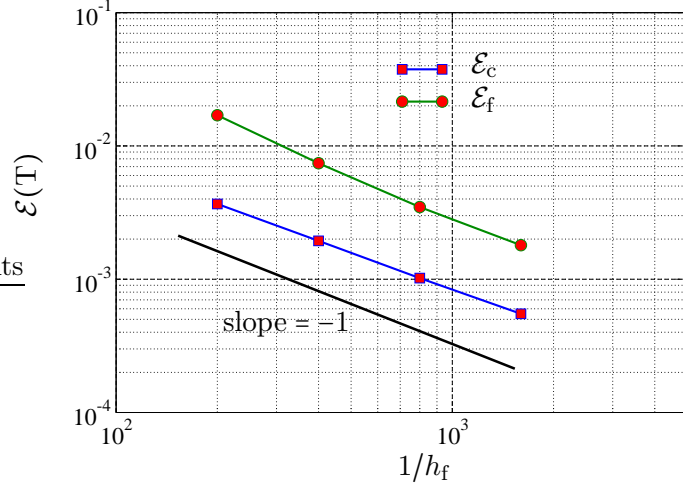


FIGURE 14. Advection and diffusion of one-dimensional Gaussian hill: This figure shows the error in the coarse-scale and fine-scale subdomains against refinement in the fine-scale region. Table 4 provides the numerical values employed in this numerical simulation.

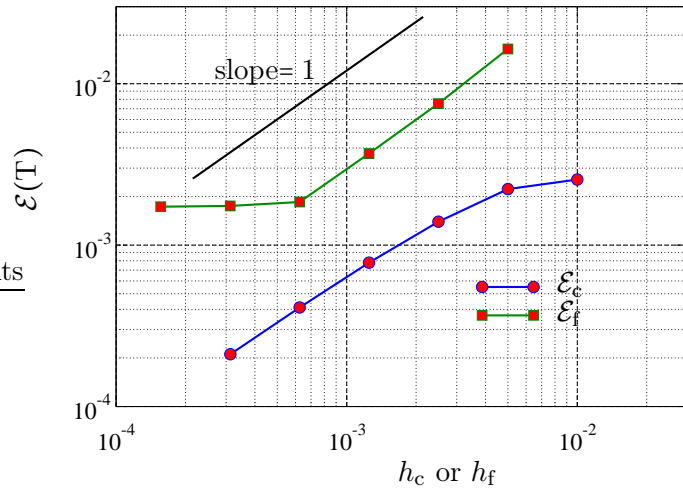


FIGURE 15. Advection and diffusion of one-dimensional Gaussian hill: The error in the fine and coarse-scale subdomains is plotted against grid-size. In all cases $h_c = 2h_f$. Grid refinement is done simultaneously in both subdomains. The ratio between the time-steps in the two subdomains is constant for all cases, $\eta = 4$. The length of the overlap region is $L = 0.04$. Parameters are given in Table 7.

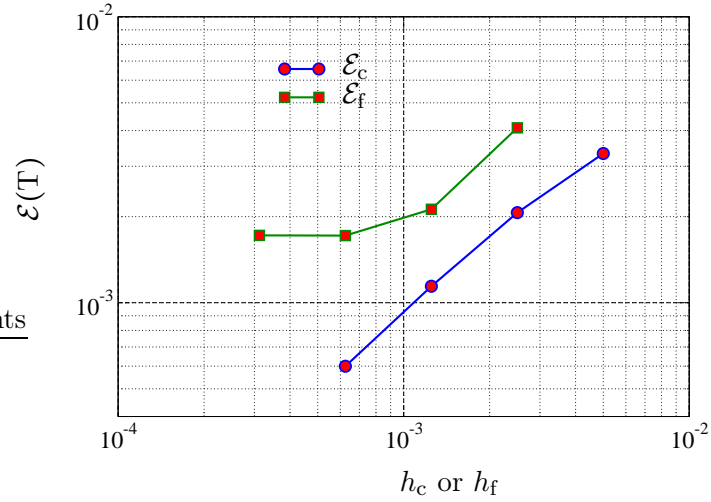


FIGURE 16. Advection and diffusion of one-dimensional Gaussian hill: In this figure, the error in the coarse- and fine-scale subdomains is shown. In this case the length of the overlap region is $L_{\text{overlap}} = 10^{-2}$.

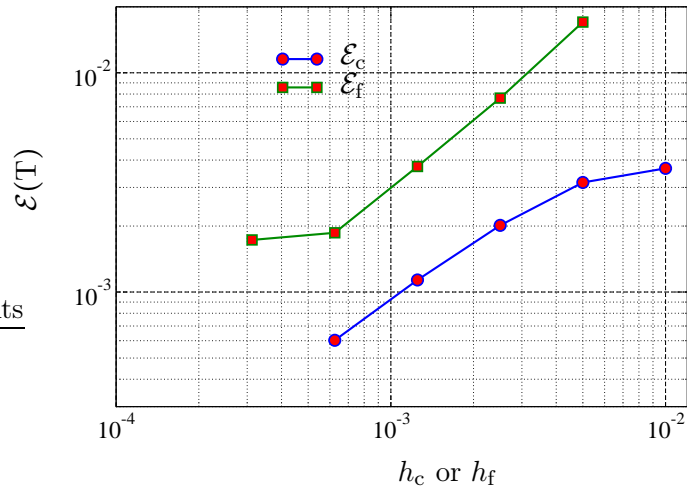
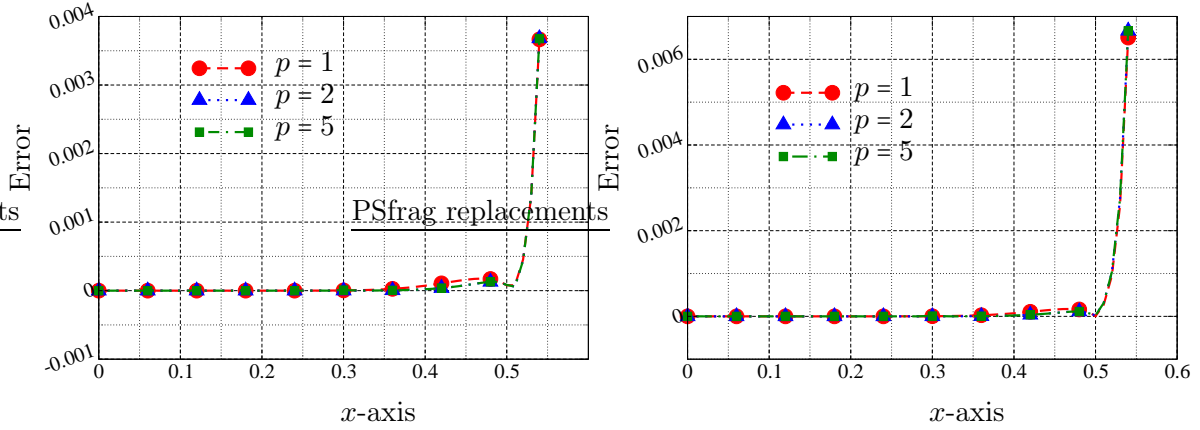
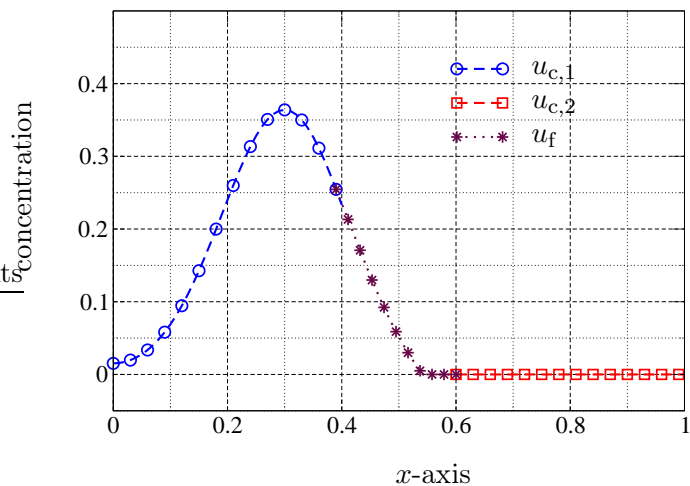


FIGURE 17. Advection and diffusion of one-dimensional Gaussian hill: Error in the fine and coarse-scale domains with respect to mesh size in each subdomain is shown. Here, the length of the overlap region is $L_{\text{overlap}} = 10^{-1}$.

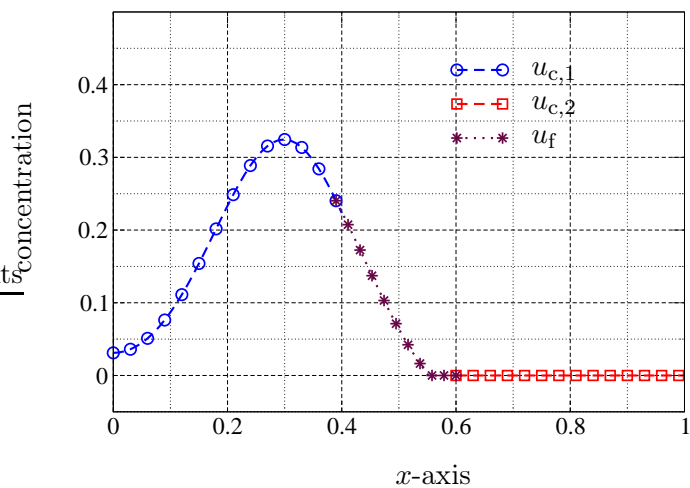


(a) $h_c = 10^{-2}$, $h_f = 5 \times 10^{-3}$, $\Delta t_c = 5 \times 10^{-3}$, $\Delta t_f = 1.25 \times 10^{-3}$ (subcycling) (b) $h_c = h_f = 10^{-2}$, $\Delta t_c = \Delta t_f = 5 \times 10^{-3}$ (no subcycling)

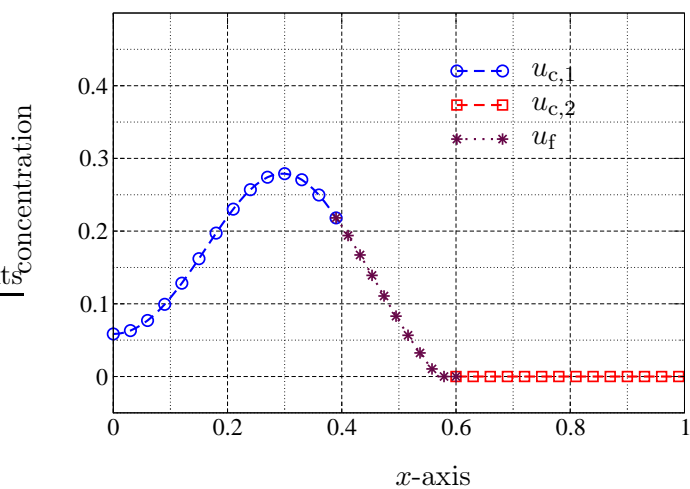
FIGURE 18. Advection and diffusion of one-dimensional Gaussian hill: In this figure, point-wise error in the coarse-scale domain at time $t = T$ is shown. Different orders of interpolation (denoted by p here) in the finite elements are used. The length of the overlap region is $L_{\text{overlap}} = 10^{-1}$. It can be observed that increasing the order of finite element interpolation does not improve accuracy near the overlap region. Moreover, the relative accumulation of the error near the overlapping region is not associated with multi-time-stepping (i.e., subcycling).



(a) $t = 0.1$

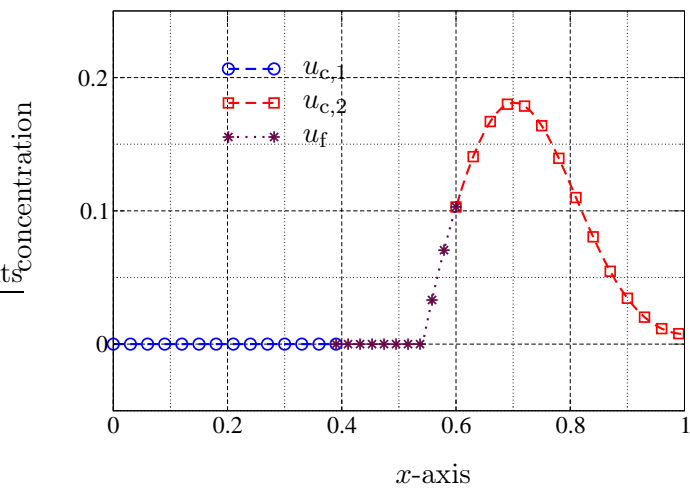


(b) $t = 0.25$

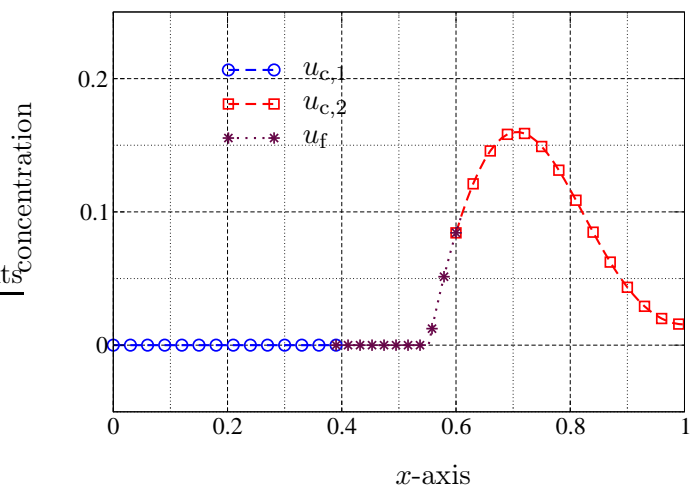


(c) $t = 0.5$

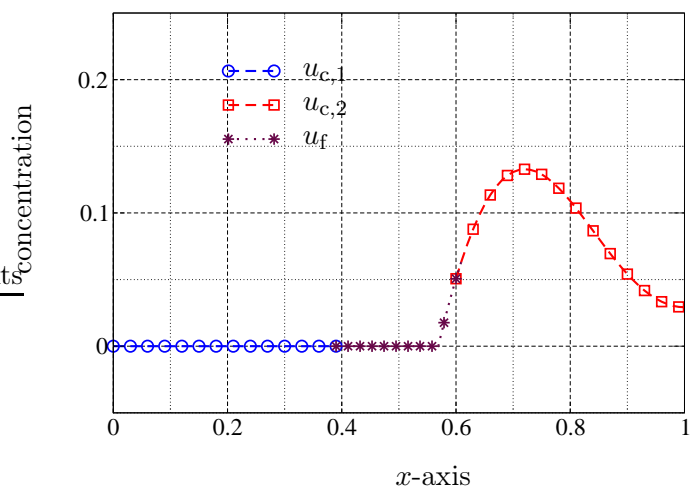
FIGURE 19. Fast bimolecular reaction in a one-dimensional domain: Concentration of chemical species A at different time-levels is shown.



(a) $t = 0.1$

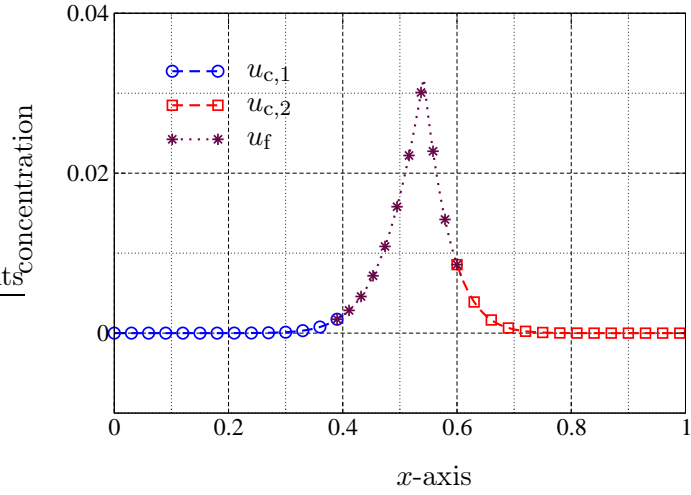


(b) $t = 0.25$

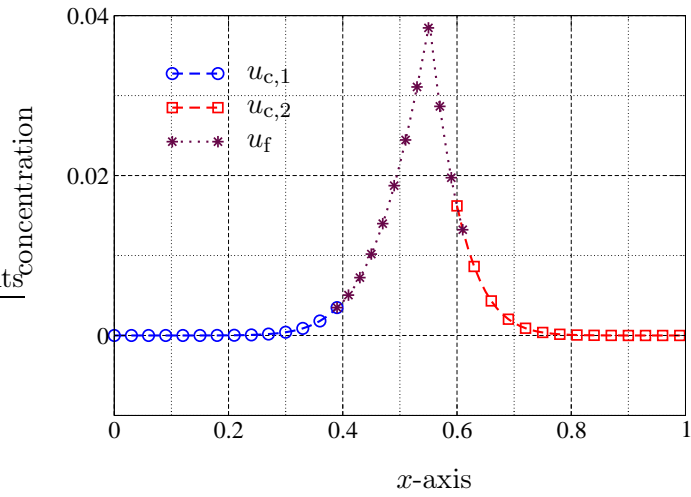


(c) $t = 0.5$

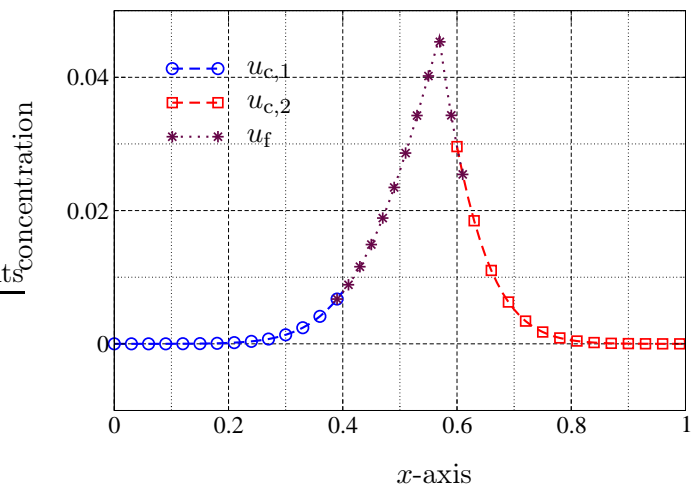
FIGURE 20. Fast bimolecular reaction in a one-dimensional domain: In this figure, concentration of species B is shown.



(a) $t = 0.1$



(b) $t = 0.25$



(c) $t = 0.5$

FIGURE 21. Fast bimolecular reaction in a one-dimensional domain: Concentration of species C is shown. The fine-scale subdomain is located near the region where majority of production occurs.

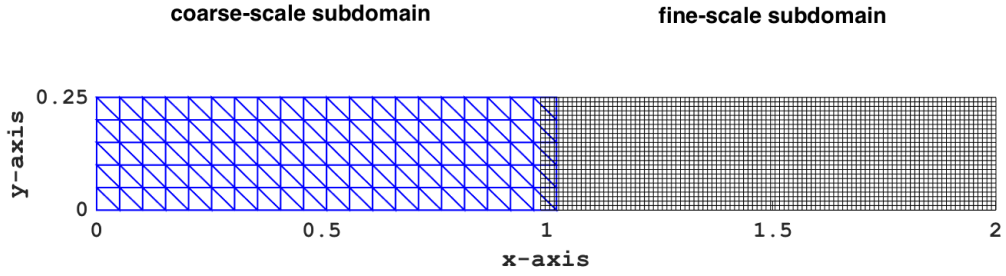


FIGURE 22. Advection and diffusion in a homogeneous medium: This figure illustrates the overlapping domain decomposition as well as the non-matching grids for coarse- and fine-scale domains. The length of the overlap region is $L_{\text{overlap}} = 4 \times 10^{-2}$.

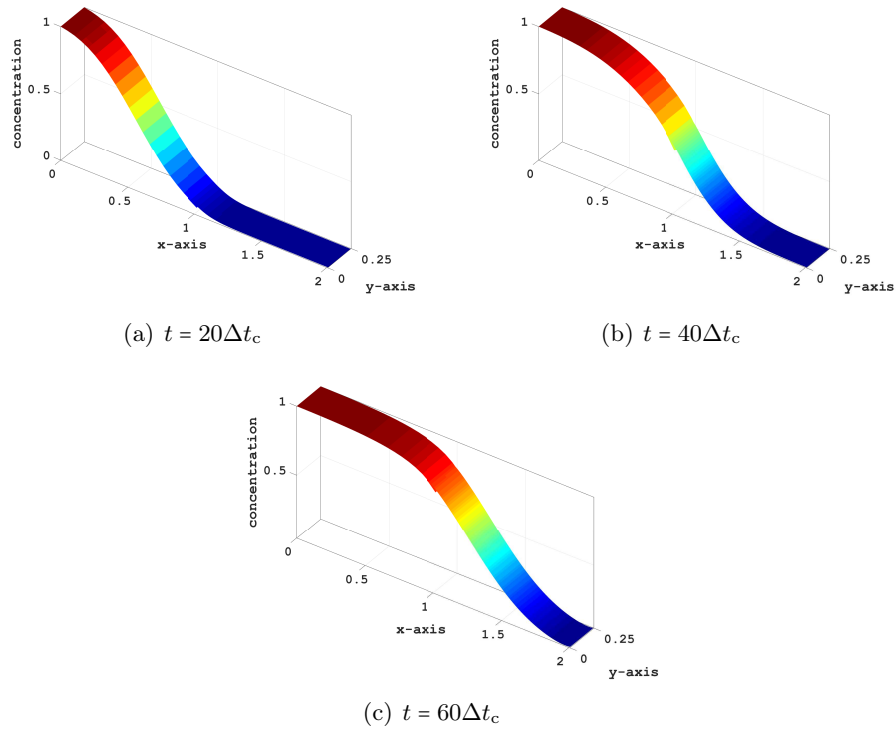


FIGURE 23. Advection and diffusion in a homogeneous medium: In this figure the concentration at different time-levels is shown. In this case Péclet number is $P = 20$. In each time-step, we have employed 5 sub-iterations to ensure the compatibility of the solution in the overlap region.

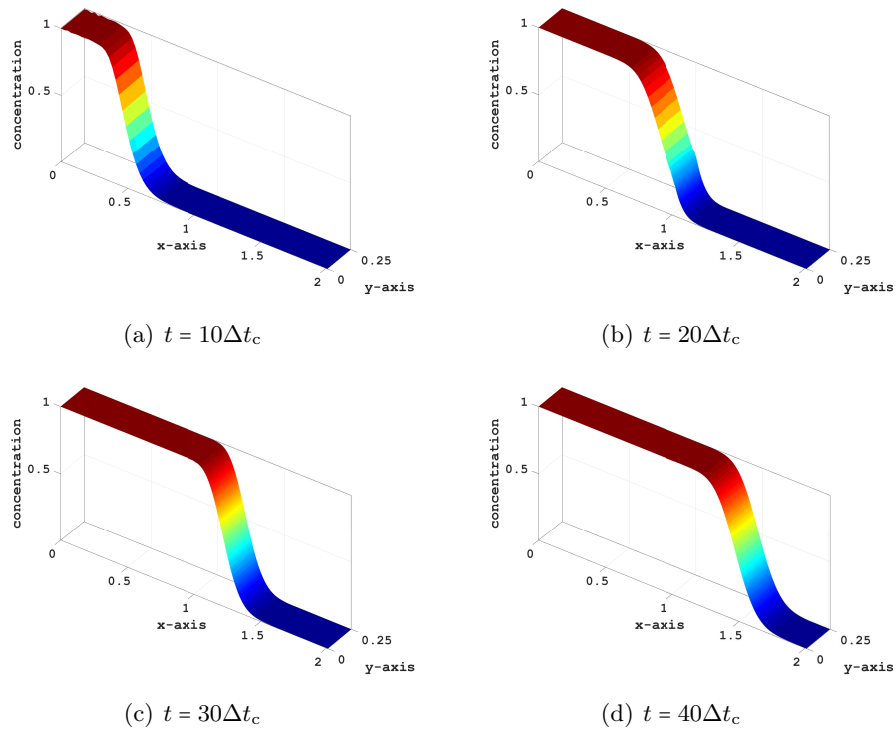


FIGURE 24. Advection and diffusion in a homogeneous medium: Concentration at different time-levels is shown. In this case Péclet number is $P = 200$. In each time-step we use 5 sub-iterations. In this case, the coupling may cause minor disruptions in the concentration profile when the front is passing through the interface. This can be improved by increasing the number of sub iterations (MaxIter). The spurious oscillations in the finite element method can be improved by mesh refinement. No spurious oscillations observed in the solution from LBM.

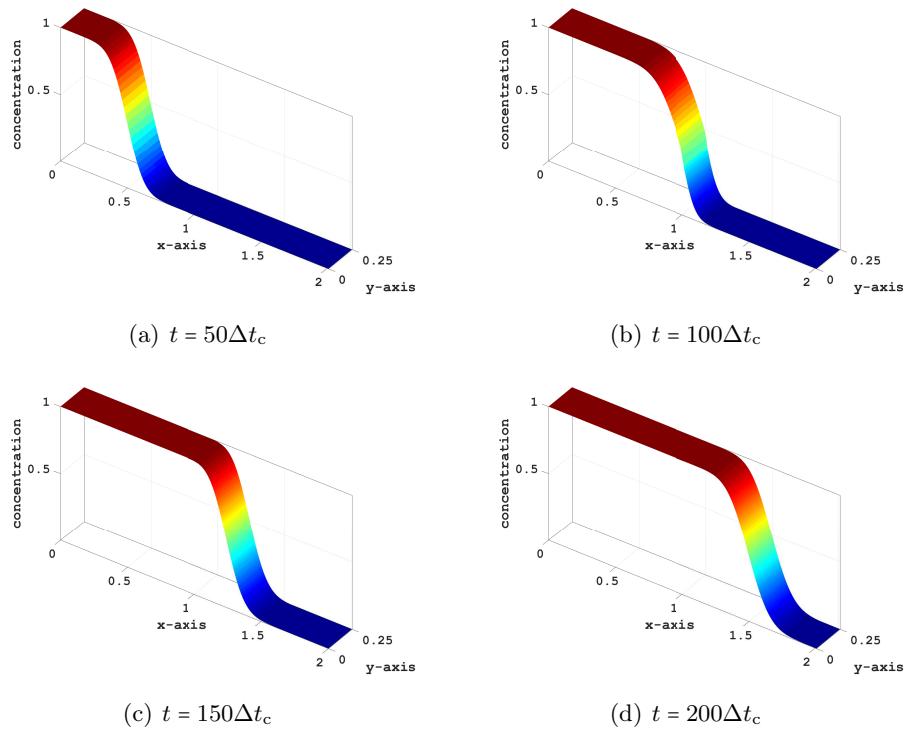


FIGURE 25. Advection and diffusion in a homogeneous medium: In this figure, concentration at different time-levels is shown. Here, the space and time discretization is refined in order to remove spurious oscillations. The number of sub-iterations in each time-step is 10, which has helped reduce the incompatibility in the overlap region.

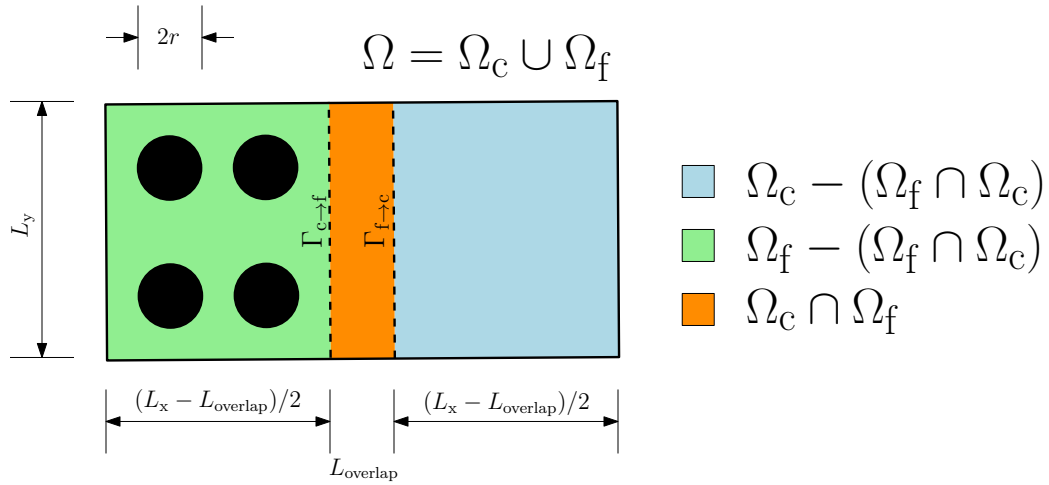
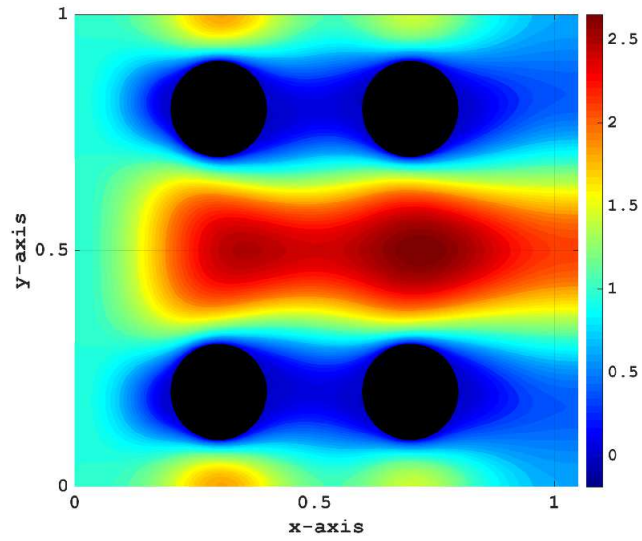
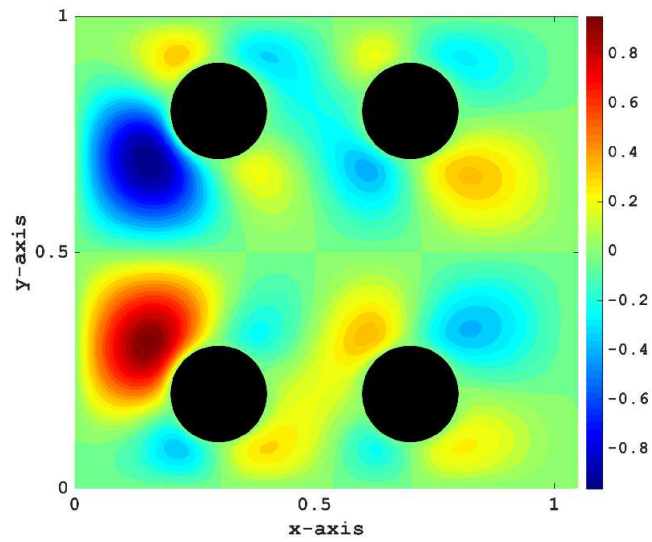


FIGURE 26. Dissolution of calcite problem: Computational domain and its decomposition into fine and coarse-scale subdomains are shown. The black circles represent the solid phase in the porous medium.



(a) velocity in the x-direction



(b) velocity in the y-direction

FIGURE 27. Two-dimensional problem: The velocity field shown in this figure is obtained using a lattice Boltzmann simulation of incompressible Newtonian fluid. The black circles represent the solid obstacles in the porous medium.

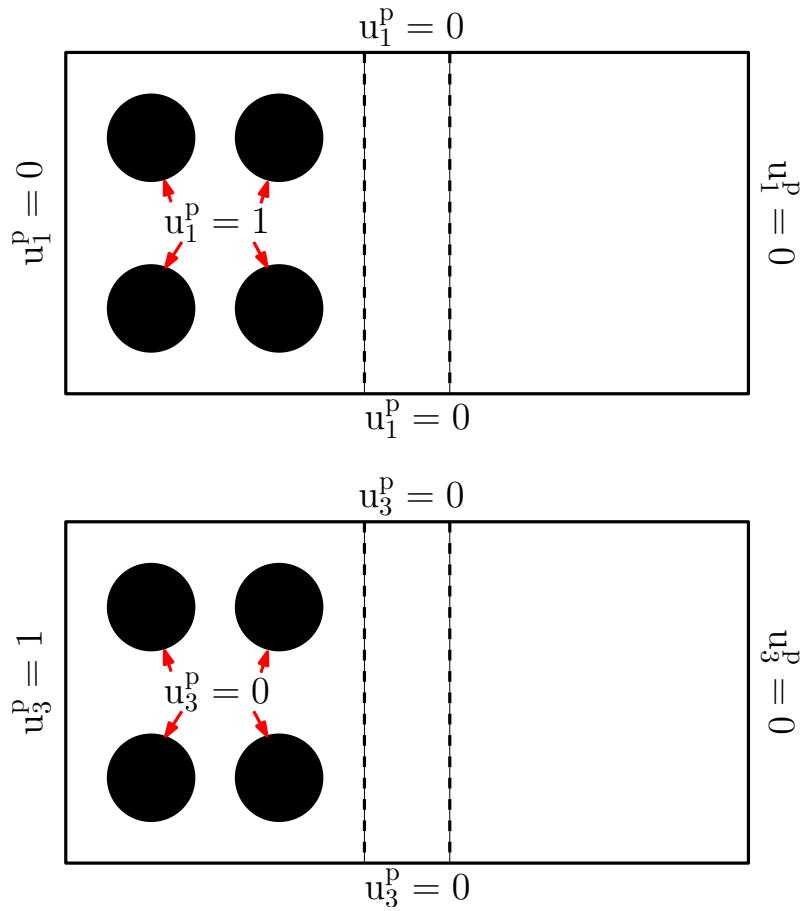


FIGURE 28. Dissolution of calcite: The boundary conditions for the simulation of dissolution of calcite in the porous medium are shown.

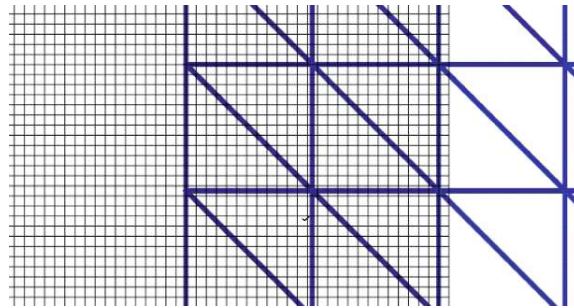
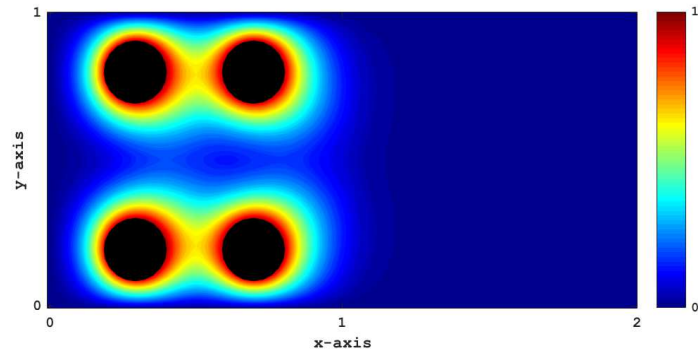
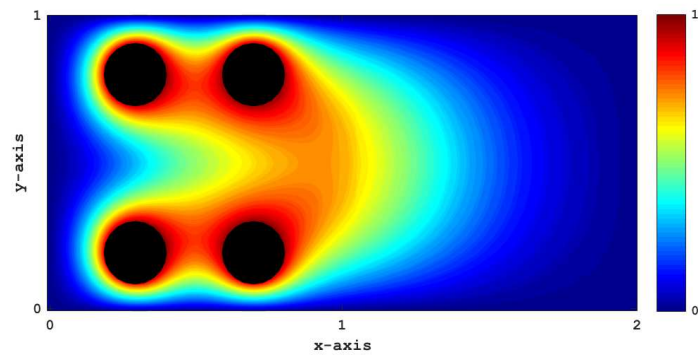


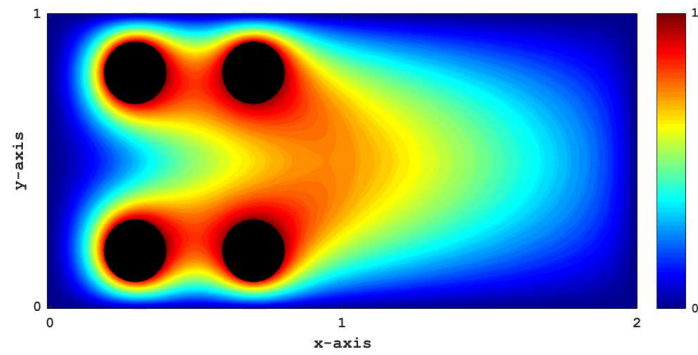
FIGURE 29. Dissolution of calcite: This figure shows the finite element mesh (which is indicated using triangular elements) and the lattice for LBM analysis (which is indicated by square cells) near the overlapping interface.



(a) $t = \Delta t_c$

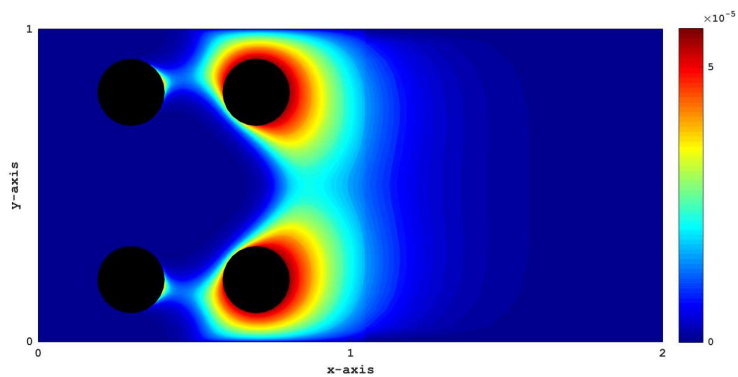


(b) $t = 5\Delta t_c$

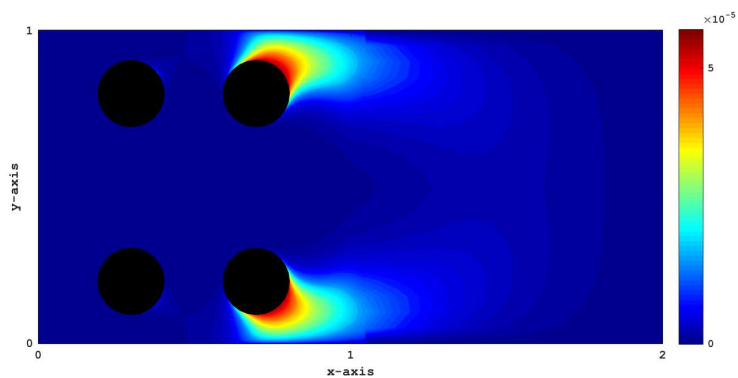


(c) $t = 10\Delta t_c$

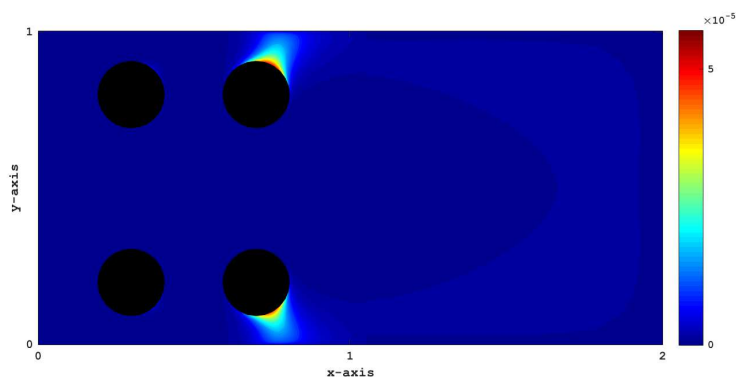
FIGURE 30. Dissolution of calcite: In this figure, concentration of calcite at different time-levels is shown. Initially, calcite is concentrated near the solid obstacles and is transported throughout the domain at later times.



(a) $t = \Delta t_c$

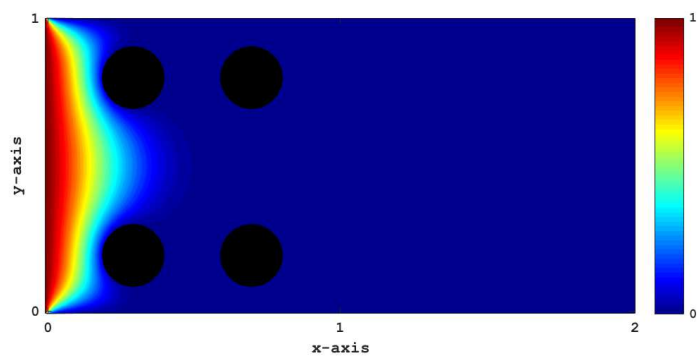


(b) $t = 2\Delta t_c$

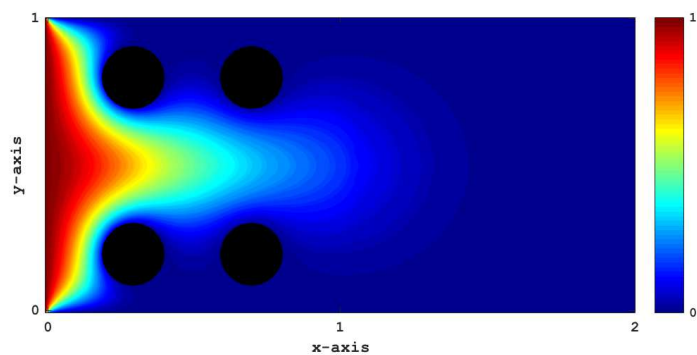


(c) $t = 3\Delta t_c$

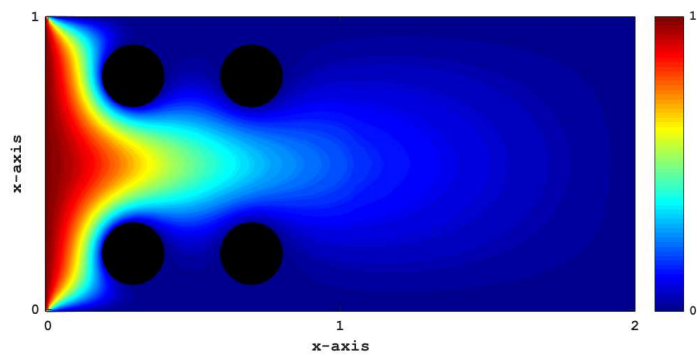
FIGURE 31. Dissolution of calcite: In this figure, concentration of Ca^{2+} is shown. It can be observed that in the first time-steps, concentration of this chemical species is more spread out in the spatial domain. At later time-levels, due to stronger presence of other participating chemical species, Ca^{2+} is largely dissolved and precipitates near the solid obstacles (shown as black circles).



(a) $t = \Delta t_c$



(b) $t = 5\Delta t_c$



(c) $t = 10\Delta t_c$

FIGURE 32. Dissolution of calcite: Concentration of the CO_3^{2-} is shown at different time-levels. This chemical species is often in solute form. As it can be seen in these figures, the transport within the pores is largely hindered due to presence of calcite, which is shown in figure 30.

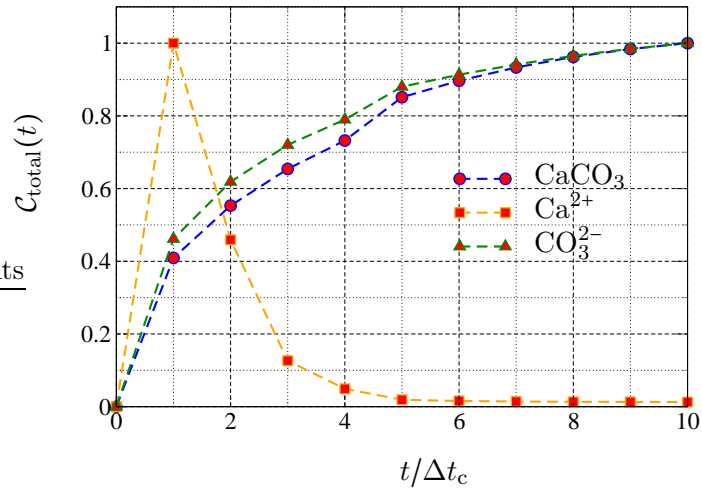


FIGURE 33. Dissolution of calcite: This figure shows the variation of the total concentration in the entire domain of each participating chemical species with respect to time. The concentration of Ca^{2+} decreases as the concentrations of CaCO_3 and CO_3^{2-} increase in the domain. The values shown here are normalized with respect to the maximum total concentration of respective species.